https://doi.org/10.5194/egusphere-2026-3219
Preprint. Discussion started: 24 June 2026

Assessing SWOT performance to measure waves and sea level variability over Rangiroa atoll, French Polynesia

Ewen Cottour[1], Guillaume Dodet[1], Clémence Chupin[2], Laurent Testut[3], Taina Postec[1], Lisa Maillard[1,4], Swen Jullien[1], and Frédéric Bouchette[5]

[1]Univ. Brest, CNRS, IRD, Ifremer, Laboratoire d'Océanographie Physique et Spatiale (LOPS), IUEM, Brest, 29200, France
[2]ENSTA/Institut Polytechnique de Paris, Lab-STICC, Equipe M3, UMR 6285, Brest, 29200, France
[3]CNRS/La Rochelle Université, LIttoral ENvironnement et Sociétés (LIENSs), UMR 7266, La Rochelle, 17000, France
[4]University of Montpellier, CNRS, Montpellier, France
[5]Centre national d'études spatiales (CNES), France

Correspondence: Guillaume Dodet (guillaume.dodet@ifremer.fr)

Abstract. Atoll reef islands are highly vulnerable to climate change because of their low elevation, exposure to ocean swells, and dependence on coral reef health. However, Sea Surface Height (SSH) and Significant Wave Height (SWH) variability across large atolls remain poorly documented due to limited in-situ observations. Satellite altimetry offers strong potential for monitoring these environments. In particular, the Surface Water and Ocean Topography mission (SWOT), through its Ka-band Radar Interferometer (KaRIn), enables two-dimensional observations of SSH and SWH at unprecedented resolution, offering new opportunities to investigate the barrier-reef lagoon dynamics of atoll islands. Yet, the performance of SWOT observations in such complex coastal settings must first be assessed. In this study, we compare KaRIn measurements with wave buoy, tide gauge, and in-situ Global Navigation Satellite System (GNSS) data collected over the Rangiroa atoll in 2025. Results show that KaRIn measures lagoon SWH with a bias of 10-30 cm and a centered root mean square error (CRMSE) of 10-13 cm, outperforming the global wave model currently used to estimate Sea State Bias (SSB) in current SWOT Level-2 products. Recomputing SSB using KaRIn SWH improves SSH agreement with in-situ observations by up to 3 cm. Spatial comparisons with GNSS-derived SSH also show that KaRIn captures strong SSH gradients near the main pass and northern atoll. Finally, improved SSH anomaly fields using time-averaged KaRIn SSH reveal differences of up to 50 cm between lagoon and ocean water levels driven by wave and tidal forcing.

1 Introduction

Atolls are ring-shaped coral reef formations that have developed primarily in the tropical Pacific and Indian oceans through cyclic Quaternary sea-level fluctuations that drove karst dissolution on the central part of flat-topped carbonate banks and subsequent coral-reef growth along their margins, according to the revisited antecedent karst theory by Droxler and Jorry (2020). With their current low elevation and direct exposure to oceanic forcings, atoll islands are particularly vulnerable to extreme wave events, rapid sea level rise and coastal flooding (Andréfouët et al., 2023). For instance, Storlazzi et al. (2018) anticipate that most atoll islands will become uninhabitable by 2050 due to the reducing availability of freshwater resources

https://doi.org/10.5194/egusphere-2026-3219
Preprint. Discussion started: 24 June 2026

caused by sea level rise and the more frequent wave-induced overwash events. Moreover, a massive loss of warm water coral reefs is expected by the mid century due to the ocean warming and acidification simulated for a global warming of 2.0°C above pre-industrial levels (Hoegh-Guldberg et al., 2018). Given the critical role of barrier reef on swell dissipation (e.g. Sous et al., 2020), this expected degradation of reef environment is expected to enhance the vulnerability of many atoll islands. It therefore appears fundamental to strengthen our environmental monitoring capacity in these remote environments.

In-situ observations of sea level within atolls are limited because installing and maintaining long-term monitoring instruments is particularly challenging in these environments, due to their complex morphology, remoteness and limited suitable locations along the atoll rim. Only a few tide gauges are installed on atoll islands, providing limited information on local sea level variability in the lagoon nearby the atoll rim. Therefore, satellite altimetry represents a great opportunity to upscale atoll sea level monitoring. However, conventional altimetry measurements suffer from land contamination in coastal areas - such as the barrier reef enclosing the lagoon - where the back-scattered signal is disturbed by interference from land in the radar footprint (Vignudelli et al., 2011). As a result, comparisons between distant altimetry and tide gauge records require a careful methodology to minimize the errors induced by the spatial distance between the measured values (Bonnefond et al., 2019). To overcome these limitations, in-situ Global Navigation Satellite System (GNSS) measurements can be used for measuring sea level away from the coast and performing the necessary calibration and validation (CAL/VAL) of new satellite missions (Chupin et al., 2020; Lycourghiotis and Kariotou, 2022). GNSS-based methods are particularly valuable because they allow accurate measurement of the ellipsoidal Sea Surface Height (SSH) without land contamination, which is directly comparable to satellite altimeter data. For instance, several studies at established CAL/VAL sites, such as the Corsica calibration site (Bonnefond et al., 2025), demonstrate the potential of combining GNSS measurements, tide gauge records, and satellite altimetry to assess long-term altimeter biases in complex coastal areas. More recently, a field campaign conducted in the Noumea lagoon extended for the first time these CAL/VAL approaches to a barrier-reef lagoon environment, highlighting their applicability in reef-lagoon systems (Chupin et al., 2023).

The advent of wide-swath altimetry, with the launch of the Surface Water and Ocean Topography (SWOT) satellite mission in December 2022, represents a major opportunity to collect 2D high-resolution SSH data over atolls. Its main instrument is the Ka-Band Radar Interferometer (KaRIn), a new sensor capable of measuring SSH, wind speed and significant wave height (SWH) over a swath of 120-km width, with a horizontal resolution of 250 m (in its Low Resolution mode). Due to its high horizontal resolution and swath coverage, KaRIn can provide many more valid measurements than conventional altimeters in complex coastal areas (Peral et al., 2024). Based on comparisons between SWOT and CryoSat-2 against tide gauges in the Bristol Channel, Lichtman et al. (2025) showed that KaRIn SSH achieves root mean square differences (RMSD) ranging from 5.9 to 15.0 cm, while CryoSat-2 RMSD reaches about 17.0 cm in this area. For SWH, using a comparison with GNSS buoys in Bass Strait, Hay et al. (2025) reported a KaRIn SWH bias of about 6 cm and a Centered Root Mean Square Error (CRMSE) of 21 cm in coastal areas. A few recent studies have demonstrated the potential of SWOT measurements to investigate atoll dynamics (Postec et al., 2026; Rebouillat et al., 2026). However, a detailed validation of KaRIn SWH and SSH measurements in atoll environments remains to be done.

https://doi.org/10.5194/egusphere-2026-3219
Preprint. Discussion started: 24 June 2026

In this study, we analyze the performance of SWOT to measure SSH and SWH in Rangiroa (French Polynesia), the second largest atoll in the world. The combination of a long-term tide gauge operated by the French Hydrographic Service (Shom), a dedicated in-situ field campaign and the spatial coverage provided by SWOT over the lagoon makes Rangiroa an ideal location to assess SWOT's ability to measure SSH and SWH variability in the lagoon. In May 2025 a field campaign was conducted to better understand Rangiroa's dynamics and validate SWOT measurements. During this campaign, GNSS-based SSH measurements were collected throughout the lagoon. These in-situ observations provide a unique dataset to assess SWOT's ability to resolve small-scale SSH variability in the atoll environment. In this study, we compare SWOT SSH measurements with tide gauge records and GNSS-based SSH measurements. We also recompute a mean SSH field from SWOT data and validated it against the GNSS observations. Then we evaluate the performances of SWOT to measure wave height, using wave buoy records. In the next section, we present the Rangiroa atoll. Sections 3 and 4 respectively present the data used in this study, and the methods developed to process it. Results are shown and discussed in section 5. Finally, section 6 summarizes the main results and gives some perspectives.

2 Hydrodynamic and geomorphological setting of Rangiroa atoll

Rangiroa (14.14°S, 147.61°W) is the largest atoll of the Tuamotu Archipelago (Figure 1), which is part of French Polynesia in the Tropical Pacific. The atoll has a flattened elliptical shape, measuring 80 km in length and ranging from 5 to 32 km in width, with a maximum depth of the lagoon of 35 m. The atoll's rim maximum width is about 1 km, with two main passes separated by 10 km on the northern section, namely the Avatoru and Tiputa passes. They both have a depth of between 20 and 35 m, a 400-m width, and about 800-m length (Rougerie and Gros, 1980). These two passes are the main connections with the ocean and are characterized by strong tidal currents. The southern section of the atoll features hundreds of narrow and shallow channels, called hoas, where southern swells induce water fluxes towards the lagoon as a result of waves breaking over the reef top (Grimaldi et al., 2022; Andréfouët et al., 2022). It is classified as a semi-open atoll, with a degree of aperture of 0.22 which means that 22% of the rim length is made of either tidal passes, spillways or sub-tidal or intertidal reef flats (Andréfouët et al., 2001).

Rangiroa lagoon has a micro-tidal tidal regime, with a mean tidal range of around 25 cm within the lagoon (Shom, 2022). The low tidal range is primarily due to the absence of continental margin and associated tidal amplification and the proximity (about 600 km) of Rangiroa to a M2 amphidromic point (Dumas et al., 2012). The regional wind climate is dominated by southeasterly trade winds (Dutheil et al., 2020) all year long. Rangiroa open ocean is submitted to three wave regimes: trade wind waves present all year long (SWH 1-1.5m, Peak period, Tp 8-9s), south-southwest swells (SWH 2-3m, Tp 14-15s) originating from the Southern Ocean all year long but with an increased frequency during austral winter, and north-western swells (SWH 1.5m, Tp 14-15s) originating from the North Hemisphere storms in austral summer (Dutheil et al., 2021). Within the atoll, the sea state is primarily controlled by locally generated wind waves associated with the trade winds.

https://doi.org/10.5194/egusphere-2026-3219
Preprint. Discussion started: 24 June 2026

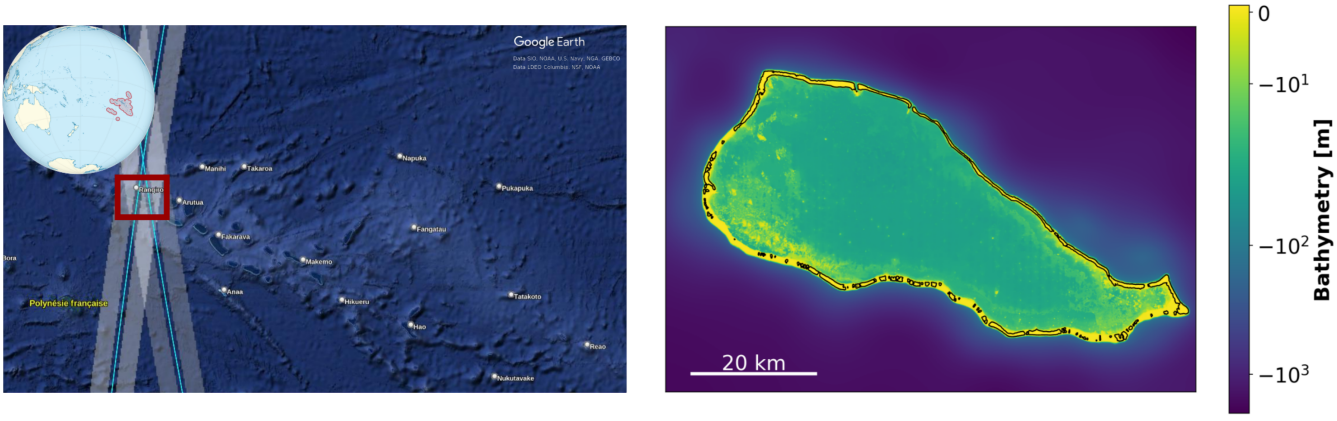

Figure 1. (Left panel) Google Earth image of the Tuamotu archipelago (© Google Earth imagery. Map data © Google. Data providers include SIO, NOAA, U.S. Navy, NGA, GEBCO, LDEO-Columbia, NSF, and NOAA) with SWOT tracks 388 and 485 superimposed as dimgrey regions. (Right panel) Satellite view of Rangiroa atoll with the bathymetry in color. Bathymetric data are inverted from Sentinel-2 imagery (courtesy of J. Lefèvre, IRD/ENTROPIE).

3 Data

3.1 FUTURISKS 2025 field campaign

In May 2025, a field campaign was conducted in Rangiroa as part of the ANR PPR FUTURISKS project (https://futurisks.recherche.univ-lr.fr/en/projet-en/), whose objective is to understand and mitigate coastal risks in Tropical French Overseas Island Territories. During this campaign, a unique database of hydrodynamic and morphological information was collected to investigate the atoll circulation and flooding risks during extreme events. For this purpose, the deployment of several hydrodynamic instruments was carried out within the lagoon, in the Avatoru pass, over the reef top, and outside the lagoon over the reef slope. Specific deployments with GNSS-based sea level measuring instruments were carried out to assess the performance of SWOT KaRIn SSH measurements. In addition, two wave buoys were deployed to evaluate the performance of KaRIn SWH measurements.

3.1.1 GNSS instrumentation

During the FUTURISKS field campaign, two GNSS-systems were used to measure the ellipsoidal Sea Surface Height (SSH) in Rangiroa lagoon. The first instrument is a GNSS buoy, specifically designed for altimetry CAL/VAL activities (Born et al., 1994; Bonnefond et al., 2013). This buoy is a prototype instrument jointly developed by the laboratory "Littoral Environnement et Sociétés" (LIENSs) and the Technical Division of the Universe Science French Institute (DT-INSU). It consists of a GNSS antenna (Leica AR10) fixed to the vertical axis of a floating structure, with a metal cylinder containing the receiver (Septentrio PolarX5 recording at 1Hz) and batteries (Figure 3 b). This buoy was deployed for two periods of 76 and 24 hours respectively,

https://doi.org/10.5194/egusphere-2026-3219
Preprint. Discussion started: 24 June 2026

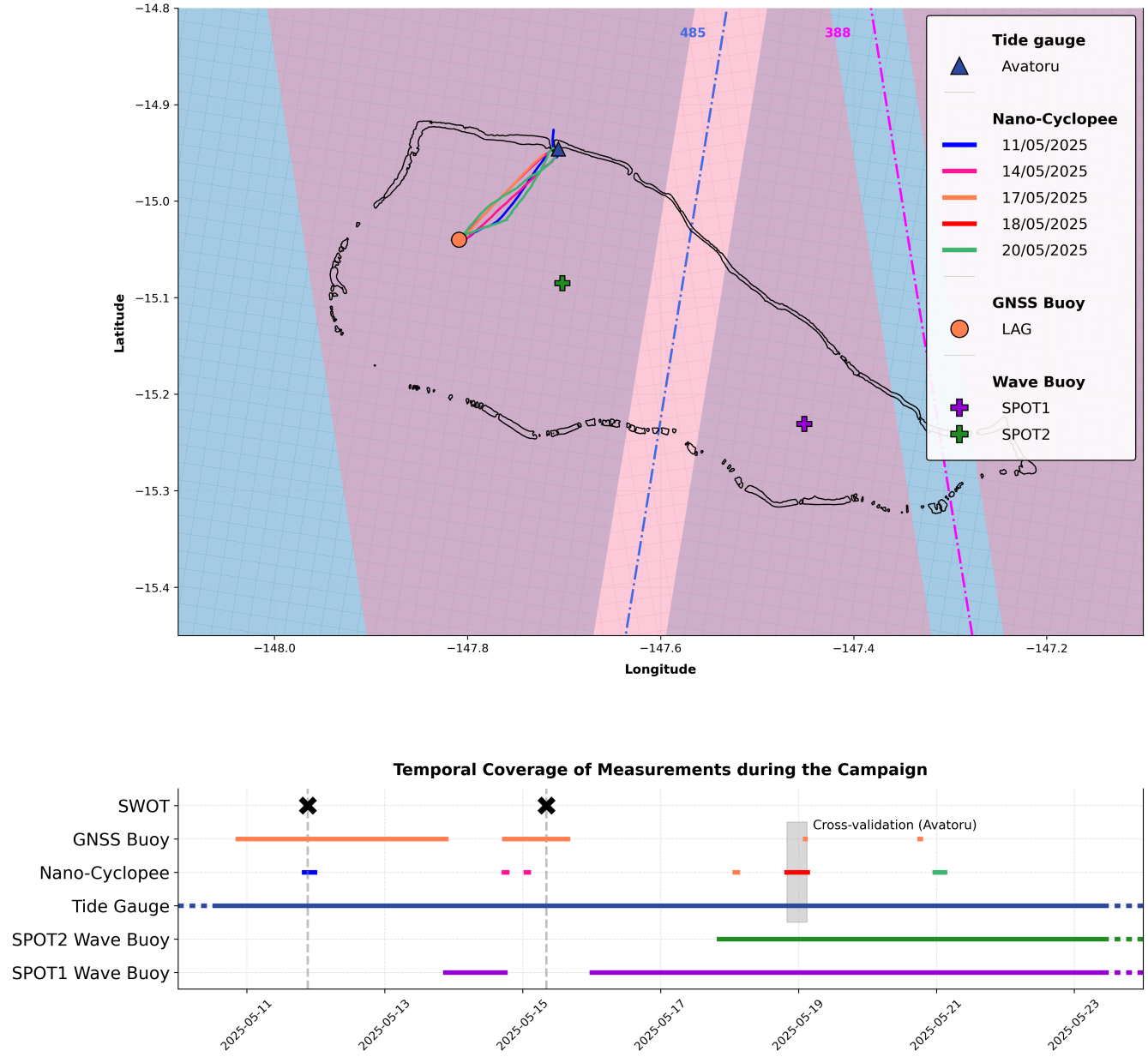

Figure 2. (Top panel) Locations of in-situ sensors (tide gauge, GNSS buoy, Nano-Cyclopée tracks, wave buoys) overlaid with SWOT ascending and descending swaths over the lagoon (namely tracks 388 & 485, pinkish and bluish areas); (Bottom panel) Timeline of acquisitions for each measurement system during the FUTURISKS Rangiroa field campaign, in May 2025.

https://doi.org/10.5194/egusphere-2026-3219
Preprint. Discussion started: 24 June 2026

each comprising one SWOT overpass, at a fixed position (named LAG hereafter) in the lagoon approximately 15 km from the Avatoru pass (see Figure 2).

The second system is named Nano-Cyclopée. It is also a prototype instrument jointly developed by the LIENSs laboratory and DT-INSU (Chupin et al., 2020). It consists of a GNSS antenna (Leica AR10), and a GNSS receiver (Septentrio PolarX5 recording at 1Hz), coupled with an acoustic altimeter (Senix Corporation Toughsonic 14 ultrasonic sensor, 10Hz). The acoustic altimeter is used to compute the air draft between the sea surface and the GNSS antenna (Chupin et al., 2020) (Figure 3 c). The Nano-Cyclopée can be installed on a boat, allowing kinematic measurements of SSH. During the two-week field campaign, a dedicated survey synchronized with a SWOT overpass (May 11) was carried out along a transect in the Avatoru pass, and seven transects were monitored between Avatoru and the LAG position, in order to compare mean SSH profiles with SWOT measurements (Figure 2).

On May 18, a dedicated cross-validation session was carried out with the GNSS buoy and the Nano-Cyclopée deployed next to the Avatoru tide gauge (Figure 3 a). These measurements were performed in order to estimate noise level and vertical offsets between the instruments.

3.1.2 Wave Buoy data

In addition to GNSS instruments, two wave buoys (Figure 3 d) were deployed to measure wave parameters inside the Rangiroa lagoon (Figure 2). We used Spotter buoys, which are low-cost, real-time, solar-powered wave measurement buoys, developed by Spoondrift Technologies, Inc. (www.spoondrift.co). These buoys were deployed with a mooring line to record wave parameters at a fixed location. The first one was deployed on May 13, 2025 in the eastern part of the lagoon at a depth of 25 m (SPOT1), and the second one was deployed on May 16, 2025 in the western part of the lagoon at a depth of 27 m (SPOT2). These buoys collected data over three months, until August 15, 2025.

The wave buoy parameters are derived from the variance-density spectrum computed over each 30-min record using the official Sofar Ocean parsing script (Sofar, 2019). For each 30-min recording period, SWH, as well as the mean and peak wave period and wave direction, are derived from spectral quantities following the definitions provided in the Sofar Ocean documentation (Sofar, 2021).

3.2 Avatoru tide gauge

To measure water level variations in the lagoon, the Shom maintains a tide gauge in the Avatoru marina (blue triangle on figure 2) since February 2009 (SHOM, 2024). This tide gauge consists of a radar sensor (VEGAPULS 62) coupled with a pressure sensor (Keller PR-36 XW) in case of radar sensor failure (Lannuzel, 2010). A co-located GNSS antenna (TRIMBLE ALLOY GNSS receiver and TRIMBLE ZEPHYR 3 GNSS antenna) was installed on February 26, 2009 (https://www.sonel.org/spip.php?page=gps&idStation=2269) on the roof of the tide gauge building to monitor vertical land motion. Sea level measurements from Rangiroa tide gauge are distributed by the Shom (https://data.shom.fr) quasi-continuously since February 2009 with a 1-min sampling frequency, except for a 26-month data gap between February 2021 and April 2023. In this study we use tide gauge measurements from July 2023 to January 2026, matching SWOT measurements period. Measurements from the tide

https://doi.org/10.5194/egusphere-2026-3219
Preprint. Discussion started: 24 June 2026

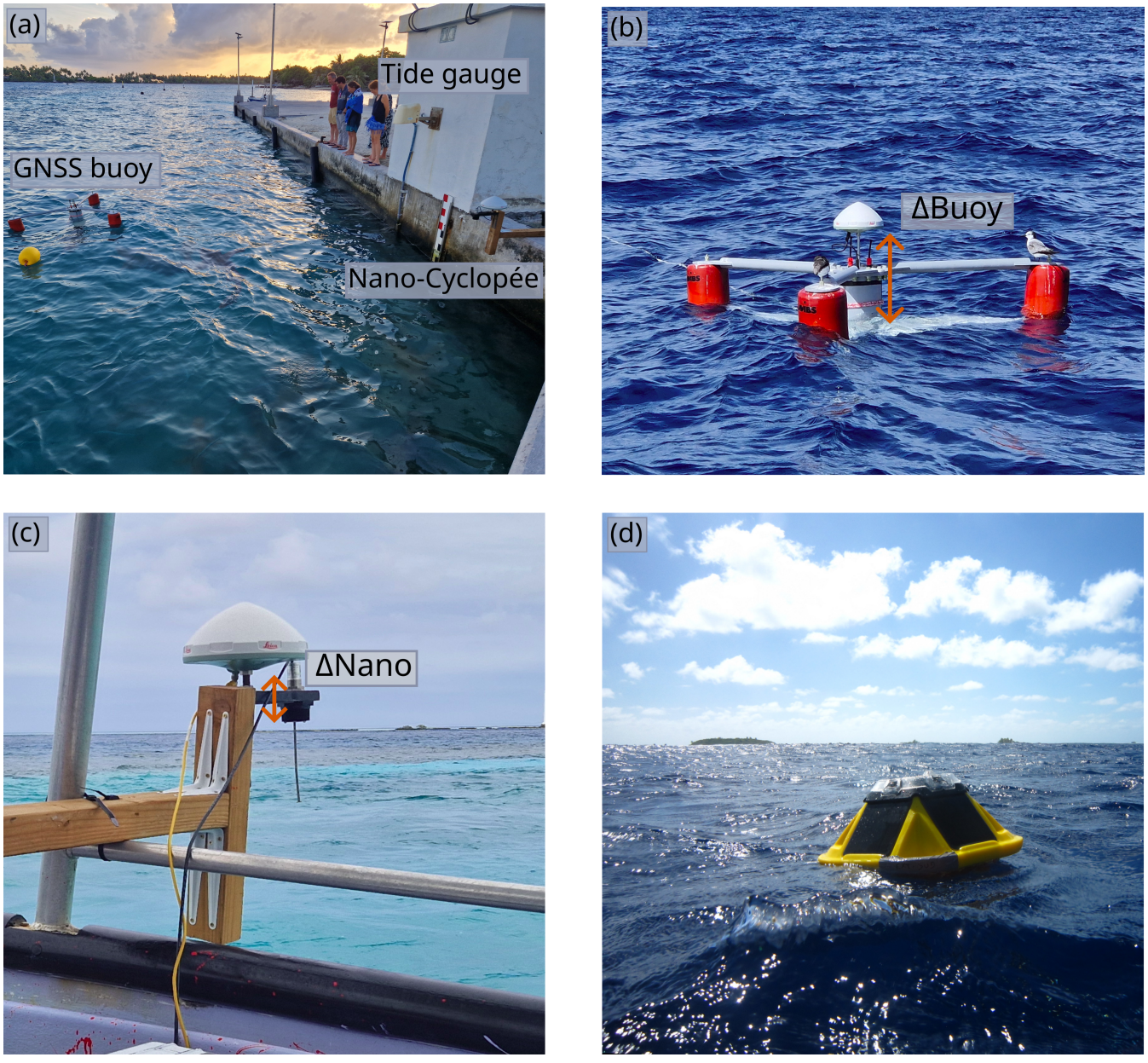

Figure 3. Photographs of in-situ instruments used in this study. (a) Tide gauge, GNSS buoy and Nano-Cyclopée during the cross-validation session held at Avatoru on May 18. (b) GNSS buoy deployed in the lagoon (LAG position). (c) Nano-Cyclopée set up on a boat. (d) Wave buoy deployed at sea. Credits: G. Dodet, S. Jullien.

https://doi.org/10.5194/egusphere-2026-3219
Preprint. Discussion started: 24 June 2026

gauge are referenced to the French hydrographic chart datum (CD), named *Zéro Hydrographique*. This datum corresponds to the theoretical level reached by the lowest astronomical tide. Several benchmarks around the tide gauge are used to monitor the vertical stability of the site and are linked to the tide gauge reference point by precise GNSS leveling. One of these benchmarks has been positioned with respect to the GRS80 ellipsoid using GNSS measurements processed in Precise Point Positioning (PPP) mode, linking the Chart Datum CD to the ellipsoid (Shom, 2023). Hence, tide gauge measurements were linked to the ellipsoid using the following formula :

$$X_{\text{tide\_gauge/ellipsoid}} = X_{\text{tide\_gauge/CD}} + d_{\text{CD/ellipsoid}}, \tag{1}$$

with $d_{\text{CD/ellipsoid}} = 3.147$ m at Avatoru (Shom, 2023). It is important to note that this vertical offset, which is directly related to the geoid height (i.e. an equipotential surface of the Earth's gravity field), can vary considerably in this region. In the case of Rangiroa, these variations, although smaller than in the case of Tahiti (Shih et al., 2015), could reach up to several decimeters at the scale of the atoll. Moreover, the last measure of $d_{\text{CD/ellipsoid}}$ at Avatoru was made in 2023 and may include an uncertainty of a few centimeters. Indeed, this value differs (3.3 cm) from the one reported in the RAM2022 (Shom, 2022), which is based on a 2018 GNSS campaign. Such a discrepancy may arise from several factors, such as differences in reference frames and processing methods, the accuracy of the GNSS processing used, and possible vertical land motion. In the following, the tide gauge SSH will refer to the value $X_{\text{tide\_gauge/ellipsoid}}$ computed with Equation 1.

3.3 SWOT measurements

The SWOT mission is a joint project involving the American, French, Canadian and UK space agencies. Its objective is to accurately map water level of oceans, lakes and rivers to better understand the water circulation, ocean tides or river discharge (Fu et al., 2024). SWOT was launched on December 16, 2022, and from December 2022 to July 2023, the satellite was placed on a fast-repeat orbit, covering the same track every 23.8 hours. After this CAL/VAL phase, SWOT was moved to the science orbit, with a repeat period of approximately 21 days, providing a near-complete coverage of the Earth up to 79° in latitude. SWOT's two main instruments are the nadir Poseidon-3C altimeter operating in Ku-Band (12-18 GHz) and C-Band (4-8 GHZ) and the Ka-Band (26.5-40 GHz) Radar Interferometer (KaRIn) providing measurements over a 120-km wide swath, with a blind spot of 20 km at nadir (Peral et al., 2024). KaRIn is made up of two synthetic aperture radar (SAR) antennas separated by 10 meters. The radar signal is transmitted by one antenna, and echoes from Earth surface are received by both antennas. An interferometric processing of echoes enables the generation of measurements, such as the SSH. The Poseidon-3C altimeter complements KaRIn by providing data between the two swaths and a reference for correcting large-scale variations in sea level (Fu et al., 2024). The SWOT SSH is computed with respect to the ellipsoid WGS84. In addition to the topography measurements derived from the phase difference between the images acquired by each of the two antennas, KaRIn can also provide information about the sea state by exploiting the measured power in each of the SAR images and the interferometric correlation between both acquisition channels (SWOT Science Team, 2024). This last quantity, sometimes referred to as interferometric coherence, is directly affected by the presence of surface waves. This, in turn, provides an opportunity to measure, for the first time at a

https://doi.org/10.5194/egusphere-2026-3219
Preprint. Discussion started: 24 June 2026

global scale, significant wave height (SWH) at kilometric resolutions (well below the reach of nadir altimeters) and in two dimensions (Bohé et al., 2025).

In this study, we consider Level 2 (L2) KaRIn Low-Rate Unsmoothed (SWOT Science Team, 2023b) and Expert (SWOT Science Team, 2023a) data products, distributed on the AVISO data portal (www.aviso.altimetry). We use data from the descending (#388) and ascending (#485) tracks of the Science Orbit (pink and blue areas on Figure 2, respectively), from July 2023 to January 2026, which correspond to 40 cycles, that had been reprocessed with version C (PIC2, from cycle 027 to 031) and D (PGD0 from cycle 001 to 025 and PID0 from cycle 032 to 040) at the time of this study. We use Expert product (gridded at 2 km * 2 km) to obtain all standard corrections, including atmospheric, geophysical, and instrumental corrections, as well as SWH fields. We also use the Unsmoothed product to access the highest spatial resolution of SSH measurements (250 m * 235 m, see Stiles et al., 2022), which enables small scale analysis, such as inside the Avatoru pass. As this product provides only a limited number of geophysical variables, the corrections and SWH fields from the Expert product are interpolated onto the Unsmoothed grid using linear interpolation and applied to the Unsmoothed SSH. It should be noted that SWOT also provides High Rate (HR) data with high spatial resolution (10 m – 70 m depending on the pixel position from nadir) for terrestrial and coastal waters. Unfortunately, such high resolution data could not be used for this study, since small islands, such as the atolls of the Tuamotu Archipelago, were not covered by the HR mask at the time of the study.

4 Methods

The SSH corresponds to the height between the sea surface and the ellipsoid, a mathematical representation of the Earth shape. In satellite altimetry, it is derived from the range (i.e. the distance between the satellite's center of mass and the sea surface) and the satellite altitude (the distance between the satellite's center of mass and the ellipsoid). The range is derived from the time of propagation of the signal, corrected of atmospheric (wet tropospheric, dry tropospheric and ionospheric corrections) and sea state bias (SSB) effects that account for delays in the radar signal propagation and backscattering properties of a rough sea surface (Fu and Cazenave, 2001). Additionally for KaRIn instrument, a crossover correction is also needed to reduce systematic errors caused by misalignment and phase error in the two-antenna interferometric system (SWOT Science Team, 2024). We also applied geophysical corrections to the SWOT SSH to make them comparable with GNSS-based and tide gauge SSH. Indeed, GNSS-based SSH is corrected by default for the load tide, pole tide and solid earth tide (including the permanent tide). Sea level measurements made by a tide gauge installed on the land are not affected by the solid earth tide, pole tide and load tide. Hence, SWOT SSH used in this study can be written as :

https://doi.org/10.5194/egusphere-2026-3219
Preprint. Discussion started: 24 June 2026

$$
\begin{aligned}
SSH \quad = \quad & satellite\_height - range - (wet\_tropospheric\_correction \\
& + dry\_tropospheric\_correction + ionospheric\_correction \\
& + sea\_state\_bias) + crossover\_correction \\
& - (permanent\_tide + solid\_earth\_tide \\
& + load\_tide + pole\_tide)
\end{aligned} \tag{2}
$$

At the scale of the atoll, the SSH pattern is largely dominated by the shape of the geoid and by the Mean Dynamic Topography (i.e. the mean ocean circulation). The sum of these contributions are represented by the Mean Sea Surface (MSS), which can be estimated as the long-term average of the SSH, corrected of ocean tides, pole tides, solid earth tides, load tide, and atmospheric effects including the high-frequency wind effect and the inverted barometer correction (known as DAC for Dynamic Atmospheric Correction). A MSS is typically computed over periods longer than 10 years (Pujol et al., 2018; Schaeffer et al., 2023) to minimize the influence of interannual variability such as El-Nino-Southern Oscillation events. Finally, the key variable used in oceanography is the Sea Surface Height Anomaly (SSHA), which corresponds to the difference between the SSH and the MSS, corrected of tides and the DAC. The SSHA represents the dynamic component of the sea level variability. The sources and variable names extracted from SWOT products to derive SSH, SSHA and MSS parameters in this study are given in Table 1.

4.1 Reconstruction of SWOT sea level anomaly

The SSHA provided in SWOT L2 version C and D products is computed based on the CNES/CLS (2022) MSS solution, referenced to the WGS84 ellipsoid (Stiles et al., 2022). A first inspection of the SSHA revealed unrealistic patterns near the inner edge of the atoll (see Figure 9). These patterns were found to be linked to the limited resolution of the CNES/CLS (2022) MSS, which motivated the implementation of an improved mean SSH field based on the 250-m resolution SWOT Unsmoothed products. To do this, we reconstruct a local mean SSH from the average of the SSH maps. Note that in this study we call it mean SSH rather than MSS because the time period covered by SWOT (e.g. two-and-a-half years) is too short to construct a MSS product.

To compute the SWOT mean SSH, we use the corrected SSH given by Equation 2 and we apply the ("good") quality flag (Stiles et al., 2022) associated to the SSH variable in order to filter-out invalid or noisy data, induced, for instance, by rain cells. Then we compute the temporal mean using all available data for each pixel (from both ascending and descending tracks).

We compute and apply the permanent tide correction following IERS Conventions (Petit and Luzum, 2010) to be consistent with the method used for the CNES/CLS MSS (Stiles et al., 2022). This correction accounts for the static deformation of the Earth's crust due to the average gravitational pull of the Sun and the Moon. Given the negligible spatial variability of this correction at the scale of Rangiroa atoll (approximately 0.06 cm), we assume a constant value (-4.6 cm) across the atoll.

https://doi.org/10.5194/egusphere-2026-3219
Preprint. Discussion started: 24 June 2026

Variable	SWOT Product	Variable Name	Source
Geophysical Variables in SWOT Products			
SSH	Unsmoothed	–	Eq. 2
MSS	Unsmoothed	–	$\overline{SSH}$
SSHA	Unsmoothed	–	$SSH - \overline{SSH}$
SWH	Expert	`swh_karin`	Bohé et al. (2025)
SSH Corrections in SWOT Products			
Wet troposphere	Expert	`model_wet_tropo_cor`	ECMWF model
Dry troposphere	Expert	`model_dry_tropo_cor`	ECMWF model
Ionosphere	Expert	`iono_cor_gim_ka`	Global Ionosphere Maps
Sea state bias	Expert	`sea_state_bias_cor_2`	CNES
Cross-over correction	Expert	`height_cor_xover`	Stiles et al. (2022)
Permanent tide	–	–	IERS
Solid Earth tide	Expert	`solid_earth_tide`	Cartwright & Taylor (1971); Cartwright & Edden (1973)
Load tide	Expert	`load_tide_fes`	FES2022
Pole tide	Expert	`pole_tide`	Wahr (1985); Desai et al. (2015)
Dynamic atmospheric correction	Expert	`dac`	MOG2D

Table 1. Summary of SWOT geophysical variables and corrections, with their respective product associated.

Then we recompute the SSHA fields using the SWOT mean SSH ($\overline{SSH}$). Note that we do not apply the ocean and internal tide corrections, since tidal models show discrepancies in coastal systems such as atolls, due to unresolved bathymetry, narrow passes, and non-linear tidal processes (Seifi et al., 2019). We therefore assume that these tidal effects cancel out when averaged over a sufficiently long period. This point is further discussed in Section 5.3.1, where we have tested the impact of the temporal sampling on the estimated mean SSH values. The corrected SSHA is then computed using the following equation:

$$SSHA_{\text{corrected}} = SSH - \overline{SSH} \tag{3}$$

https://doi.org/10.5194/egusphere-2026-3219
Preprint. Discussion started: 24 June 2026

4.2 Sea state bias correction in SWOT data

The Sea State Bias (SSB) correction is the adjustment applied to satellite altimetry range data to compensate for the systematic underestimation of the SSH in the presence of waves partly due to the preferential reflection of radar pulses off wave troughs rather than from the wave crest. This bias, which depends on wave height and wind speed, is typically modeled using empirical or semi-empirical approaches (Tran et al., 2010). At the time of this study, the SWOT L2 products delivered on AVISO website (versions C and D) contain two SSB corrections. The first correction is derived from the nadir SWH estimate while the second correction is derived from the EC-WAM wave model (ECMWF) SWH. Both use the KaRIn wind speed (Stiles et al., 2022). In addition to these two SSB corrections, we compute a third SSB correction (hereafter referenced as SSB_KaRIn) using KaRIn SWH measurements (from L2 Expert product) and KaRIn wind speed, based on a SSB Look Up Table derived from the AltiKa measurements and currently used by CNES/CLS to improve SWOT SSB correction (Bohé, 2025).

4.3 SSH estimates from GNSS instrumentation

GNSS measurements from the Nano-Cyclopée and the GNSS buoy are processed using the NRCAN-CSRS tool from the Canadian Geodetic Survey (Natural Resources Canada, 2024). This algorithm uses a PPP method that processes GNSS measurements using precise satellite orbits and clock products to provide a position with centimeter-level accuracy. The result is referenced to the GRS80 ellipsoid. Note that differences between the two ellipsoids (GRS80 for GNSS measurements and WGS84 for SWOT) are expected to be lower than 1 mm at Rangiroa (Altamimi et al., 2023) and therefore we assume that GNSS-based SSH is directly comparable to SWOT SSH. We also tested a Post-Processed Kinematic (PPK) method, using RTKlib (Takasu, 2013). This is a differential method that requires the use of a fixed base GNSS antenna. We used the GNSS antenna set up on the roof of the tide gauge, with a frequency sampling set to 1 Hz during the campaign. However, the accuracy of the PPK method significantly decreased with the distance to the base GNSS antenna, which motivated the selection of the PPP method in this study. Comparisons between the PPK and PPP methods are presented in the appendix 6.2).

To obtain the GNSS buoy SSH, we need to remove the instrumental offset to the GNSS measurements, corresponding to the distance between the GNSS antenna reference point (ARP) and the sea surface ($\Delta\mathrm{Buoy}$ in Figure 3 b). This distance is visually estimated over repeated 30-second time period using a ruler mounted on the GNSS buoy. Given the difficulty in evaluating this distance due to the moving sea surface, this distance is estimated with an uncertainty of approximately 2 cm. To obtain the Nano-Cyclopée SSH, we also need to remove the instrumental offset to the GNSS elevation, corresponding to the distance between the ARP and the base of the altimeter ($\Delta\mathrm{Nano}$ in Figure 3 c). This offset is estimated on ground with a ruler, with an uncertainty of approximately 0.5 cm. We then remove the air draft measured by the altimeter. To compress the 10-Hz altimeter records to the 1-Hz GNSS acquisition rate and reduce instrumental noise, we compute for each GNSS timestamp the mean of the altimeter measurements within a 1-s window centered on the GNSS timestamp. Moreover, we apply a 5-minute moving average and standard deviation to the resulting GNSS-based SSH records from both the GNSS buoy and the Nano-Cyclopée in order to filter-out the short-term variability of the GNSS-derived SSH.

https://doi.org/10.5194/egusphere-2026-3219
Preprint. Discussion started: 24 June 2026

4.4 Statistical metrics used to assess measurement uncertainties

In this study, measurement uncertainties are separated into two categories: uncertainty induced by systematic effects, which affects the accuracy of the measurements, and uncertainty induced by random effects, which affects the precision of the measurements. While the latter is zero-mean by definition and can be estimated from the measured signal directly, the former needs a reference measurement against which the deviation from the true value can be estimated. In order to quantify the uncertainty associated to systematic and random effects, we use the bias and the Centered Root Mean Square Error (CRMSE), which can be written as:

$$Bias = \frac{\sum_{i=1}^{N}(M_i - R_i)}{N} \tag{4}$$

$$CRMSE = \sqrt{\frac{\sum_{i=1}^{N}[(M_i - \bar{M}) - (R_i - \bar{R})]^2}{N}}, \tag{5}$$

where M corresponds to the uncertain measurements and R corresponds to the reference measurements (assumed to be free of errors). To further investigate random noise in the SSH measurements, we also computed the standard deviation (σ) of the SSH signal from SWOT and GNSS instruments using varying spatial and time window, respectively, as detailed in the next Sections.

5 Results and Discussion

5.1 SWOT/KaRIn SWH validation

To validate KaRIn SWH within the lagoon, we compared the KaRIn SWH measurements provided in SWOT Expert products (2x2-km grid) with the wave buoy data (SPOT1 and SPOT2, figure 2) collected in the lagoon over a 3-month period. For each SWOT cycle during this period (10 cycles for SPOT1 and 8 cycles for SPOT2), we interpolated KaRIn SWH data at the two buoy locations. We also interpolated the EC-WAM model SWH data provided and used to estimate SSB corrections in standard SWOT products, in order to validate this modeled parameter. Figure 4 shows the scatter diagrams of KaRIn SWH against the wave buoy SWH at SPOT1 and SPOT2 (left panel) and EC-WAM SWH against the wave buoy SWH at SPOT1 and SPOT2 (right panel).

KaRIn SWH shows bias of 0.28 m (89.0% of the mean buoy SWH) and 0.10 m (22.2%), and a CRMSE of 0.13 m (41.2%) and 0.10 m (22.2%), at SPOT1 and SPOT2 respectively (Figure 4, left). The performance of KaRIn SWH appears to vary with sea state conditions. At SPOT1, where wave buoy SWH measurements are mostly in the range 0.2-0.4 m, KaRIn SWH exhibits a higher bias than at SPOT2, where wave buoy SWH measurements are mostly greater than 0.4 m. This behavior is consistent with previous studies showing that SWH retrievals are more challenging under low sea state conditions (Bohé et al., 2025; Turki et al., 2025). However, when comparing KaRIn SWH values for similar wave buoy SWH range, the bias at SPOT1 remains systematically higher than at SPOT2. Since Bohé et al. (2025) indicates that KaRIn SWH shows higher noise level

https://doi.org/10.5194/egusphere-2026-3219
Preprint. Discussion started: 24 June 2026

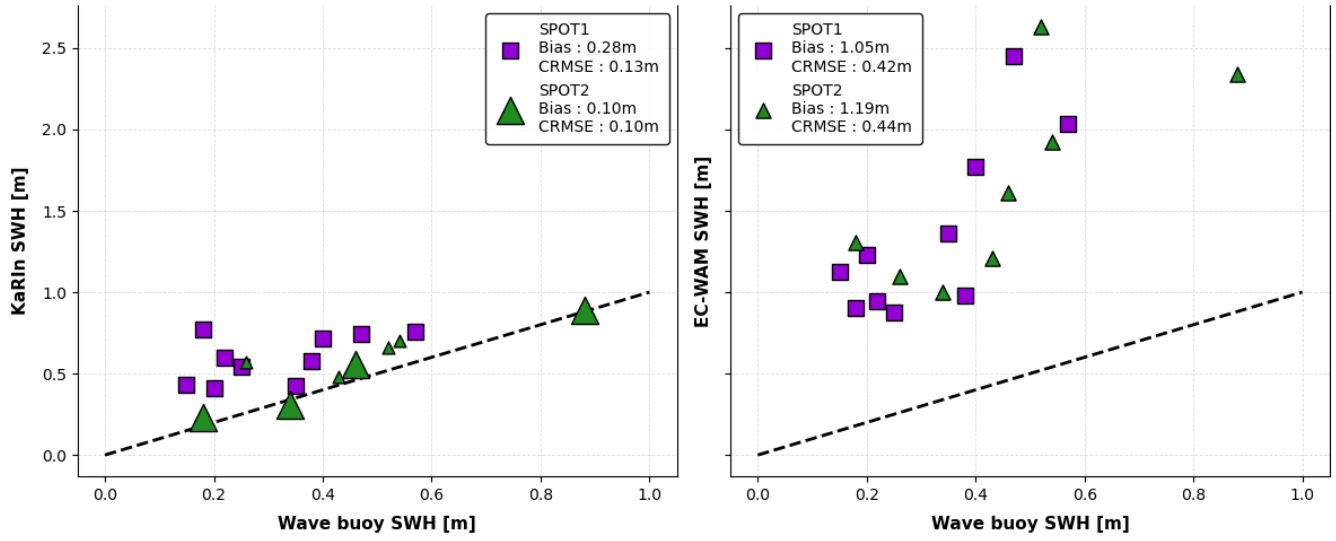

Figure 4. Scatter plots of the SWH measured by KaRIn (left panel) and the ECMWF model (right panel) versus the wave buoy estimated SWH. In the left panel, marker size qualitatively represents the cross-track distance of each wave buoy: approximately 12 km (SPOT1, SWOT track 388), 15 km (both buoys, SWOT track 485), and 40 km (SPOT2, SWOT track 388).

near the outer edge of the swaths, we computed the cross-track distance for each wave buoy. These distances are approximately 12 km (SPOT1, SWOT track 388), 15 km (both buoys, SWOT track 485), and 40 km (SPOT2, SWOT track 388). However, Figure 4 shows no clear relationship between the cross-track distance and the SWH error. This suggests that the observed bias is not driven by the position within the swath, but rather by the wave buoy itself or their location. In particular, SPOT1 is located closer to the atoll rim than SPOT2, and since the SWH is derived on the 2-km grid, land proximity could influence KaRIn SWH measurements. Despite this positive bias of KaRIn SWH for low sea states conditions, the overall error metrics indicate that KaRIn SWH provides a reliable basis to estimate the SSB over the atoll. Indeed, for a SWH bias of 30 cm (such as observed at SPOT1), the SSB overestimation is 1.2 cm, and for a SWH bias of 10 cm (matching SPOT2 SWH bias), the SSB overestimation decreases to 0.4 cm.

In contrast, EC-WAM results clearly overestimates the observed SWH, with bias against wave buoy SWH of 1.05 m (330.9%) and 1.19 m (263.0%), and a CRMSE of 0.42 m (131.7%) and 0.44 m (97.3%)), at SPOT1 and SPOT2 respectively. This indicates that the model error is dominated by a systematic overestimation. This error comes from the limited spatial resolution of global wave models. For instance, the EC-WAM wave model has a horizontal resolution of approximately 28 km (European Centre for Medium-Range Weather Forecasts (ECMWF), 2024), which corresponds to a representation of Rangiroa, the second largest atoll in the world, with only 2 or 3 grid points. At such resolutions, small islands are clearly under-resolved in global wave models and their shadowing effect on the propagation of incident swells is usually accounted for with an obstruction grid strategy (Tolman, 2003; Gaffet et al., 2025). For the specific case of atoll islands and coastal lagoons, the dramatic reduction of incident swell energy in the inner lagoon caused by sandy- or reef-barrier blocking and

https://doi.org/10.5194/egusphere-2026-3219
Preprint. Discussion started: 24 June 2026

depth-induced wave breaking (e.g. Sous et al., 2020) can hardly be parameterized without a high-resolution mesh representing fine-scale bathymetric information of the reef structure. Therefore global wave models systematically overestimate wave information in atoll and coastal lagoons. This overestimation of the SWH within the atoll propagates into the SSB correction, and finally in the SSH. This SSB error was estimated to be 3cm on average and to reach up to 7.5 cm during one SWOT overpass ($SWH_{\mathrm{model}} = 2.56$ m and $SWH_{\mathrm{KaRIn}} = 0.62m$, Figure 4). It is therefore expected that altimetry SSH and MSS are systematically overestimated in most atoll lagoon in the world, but this coastal altimetry issue has not been documented yet, to our knowledge. In the following, the SWOT SSH will be estimated using a SSB based on either SWOT measurements or in situ data.

5.2 SWOT SSH validation

5.2.1 Validation of GNSS-based SSH measurements at Avatoru tide gauge

In order to estimate uncertainty levels and vertical offset between the considered in-situ SSH measurement systems, we compared the collocated SSH data given by the tide gauge, the Nano-Cyclopée and the GNSS buoy during the cross-validation session (see Section 3.1.1). The upper panel of Figure 5 presents the measurements of the tide gauge SSH (smoothed using a 5-min moving window average), the Nano-Cyclopée SSH and the GNSS buoy SSH. The comparisons are presented as SSH on top and residual on the bottom. The Nano-Cyclopée SSH shows a bias of 0.3 cm with a CRMSE of 4.0 cm compared to the tide gauge (Table 2). This makes the Nano-Cyclopée an accurate source of measurements to assess SWOT SSH over the lagoon. Yet it is important to note that during this session the Nano-Cyclopée was set on the ground. When set on a boat, the effect of waves is expected to increase the uncertainties for both the GNSS antenna position and the acoustic altimeter measurements. Further analysis of the uncertainties in the GNSS-base measurements are given in Appendix 6.1.

The bias of the GNSS buoy is 4.7 cm and the CRMSE is 2.3 cm (Table 2). This higher bias of the GNSS buoy can be partly attributed to the low ambiguity resolution rate (about 35%) achieved by the NRCAN processing for this measurement time-period. Indeed, in GNSS positioning carrier-phase measurements involve unknown integer ambiguities, and when these ambiguities are not correctly resolved, the resulting position estimates suffer from increased noise and low-frequency errors, which directly affect the vertical accuracy. A low ambiguity resolution rate therefore leads to both larger bias and variability in the GNSS-derived SSH. In contrast, during deployments at LAG, the ambiguity resolution rate was significantly higher, reaching 90% for the first deployment and 78% for the second. Consequently, both the accuracy and precision of the GNSS buoy are expected to be improved compared to the values obtained during the cross-validation session.

5.2.2 SWOT SSH validation at Avatoru tide gauge

To evaluate the performance of SWOT SSH measurements in the lagoon near the atoll edge, we compare SWOT SSH measurements to the Avatoru tide gauge SSH. The SWOT SSH value is computed as the mean of three neighboring SWOT grid cells near the tide gauge, with a one-pixel offset (250 m) towards the lagoon to limit the presence of land portion in the SWOT pixels. As the KaRIn SWH is degraded near the coast, we used a two-pixels offset (4 km, Expert products) towards the lagoon

https://doi.org/10.5194/egusphere-2026-3219
Preprint. Discussion started: 24 June 2026

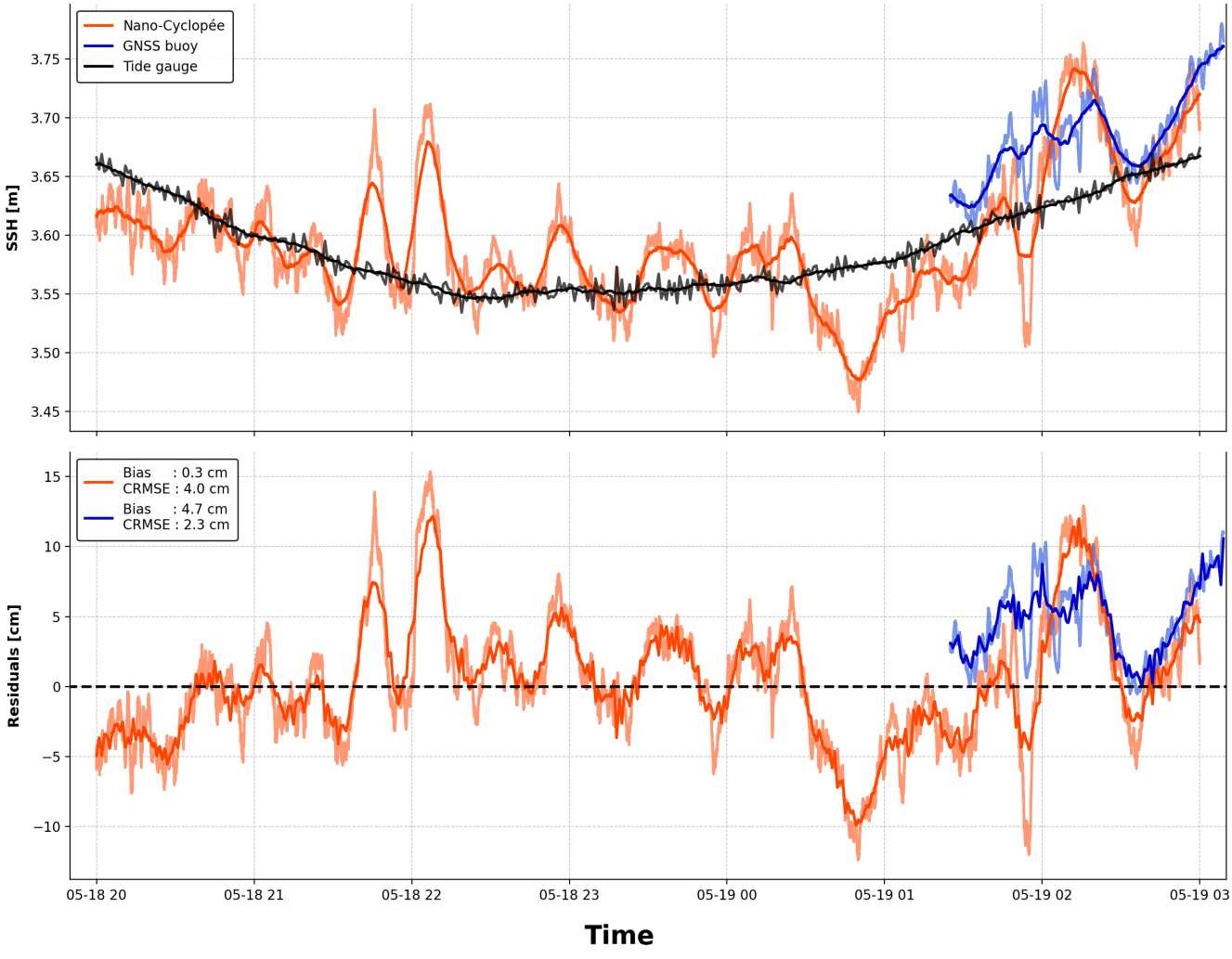

Figure 5. (Top panel) SSH time series measured by the Nano-Cyclopée (orange), the GNSS buoy (blue) and the tide gauge (black) during the cross-validation session. (Bottom panel) Residuals of the Nano-Cyclopée and the GNSS buoy compared to the tide gauge. Dark colors represent the 5-min data, pale colors represent the 1-min smoothed data.

https://doi.org/10.5194/egusphere-2026-3219
Preprint. Discussion started: 24 June 2026

Instrument 1	Instrument 2 (reference)	Bias [cm]	CRMSE [cm]
Nano-Cyclopée	Tide gauge	0.3	4.0
GNSS buoy	Tide gauge	4.7	2.3
SWOT	Tide gauge	8.6	7.3
SWOT	Nano-Cyclopée	3.6	1.8
SWOT	GNSS buoy	-2.25	1.24

Table 2. Summary of inter-comparisons between instruments, showing the bias relative to the reference measurements, and the centered root mean square error (CRMSE).

to recompute the SSB. Figure 6 (left panel) is a scatter diagram of SWOT SSH records against tide gauge records for 80 collocated values recorded during the 40 available SWOT cycles (ascending and descending tracks, from July 2023 to January 2026), with the vertical bars indicating the STD computed from the three neighboring measurements. This figure shows a clear

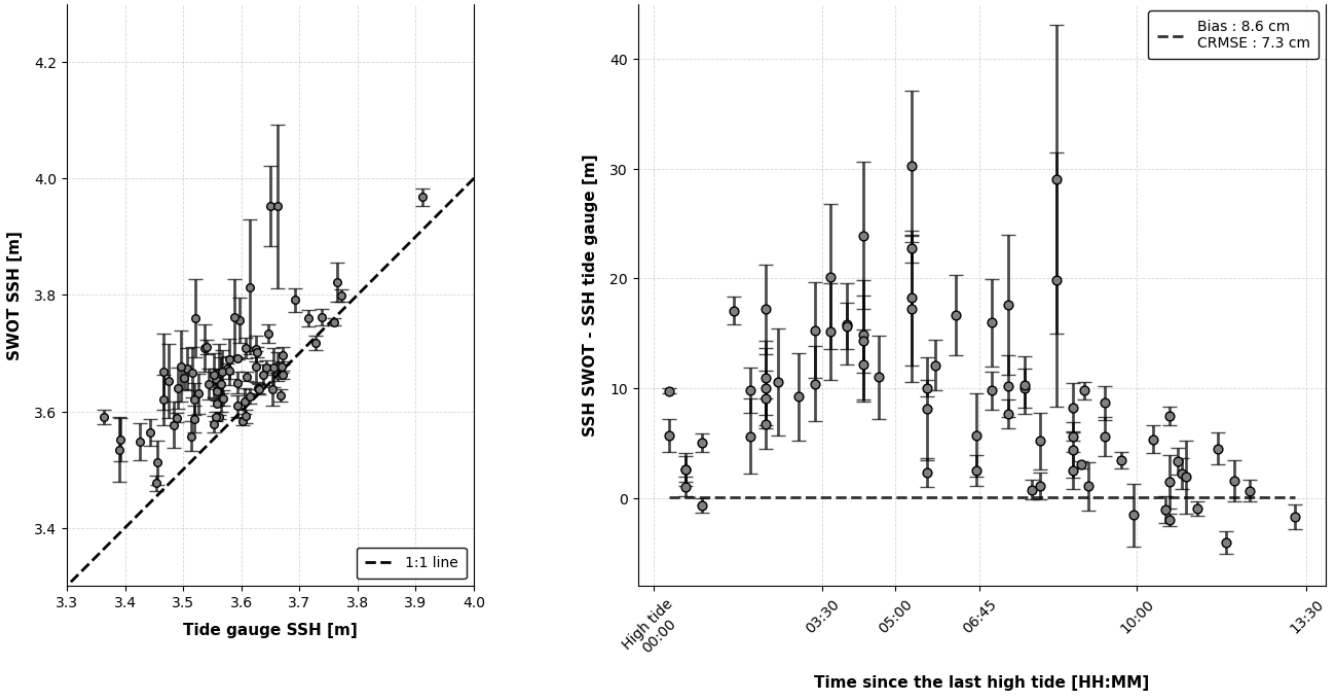

Figure 6. (Left panel) Comparisons between SWOT and tide gauge SSH measurements. Vertical bars correspond to ±1 standard deviation computed over 3 neighboring SWOT pixels; (Right panel) Differences between SWOT and tide gauge SSH as a function of the time lag with high tide.

340

overestimation of SWOT SSH data and a significant scatter across the data, with a bias of 8.6 cm, and a CRMSE of 7.3 cm

https://doi.org/10.5194/egusphere-2026-3219
Preprint. Discussion started: 24 June 2026

(Table 2). In order to investigate a possible link between the tidal stage and the differences in SWOT and tide gauge SSH, we compute the elapsed time since the previous high tide for each measurement. On the right panel of Figure 6, the difference between SWOT and tide gauge SSH is represented as a function of this time lag with previous high tide. This figure clearly shows that the largest error occurs during the ebb tide between 3 to 6 hours after the previous high tide. Conversely, the error tends to zero at high tide. The local dynamics, induced by strong tidal currents within the Avatoru pass, or the tidal fluctuation of the sea surface rugosity, might explain a few centimeters of this tidal modulation of the error. But these effects cannot explain the whole tidal modulation. Uncorrected vertical land motion or degraded correction (such as the solid earth tide or load tide) might contribute to the tidal modulation, but these assumptions have not been verified yet.

5.2.3 SWOT SSH validation in Avatoru pass and in the lagoon

While the comparison between SWOT and tide gauge SSH provides a first estimate of SWOT performance in the atoll, it only reflects SWOT's performance at a fixed location near the coast, where the presence of land and strong currents near the pass may affect the results (see section 5.2.2). To extend the validation to other locations, we used the GNSS buoy and the Nano-Cyclopée measurements to assess the performance of SWOT SSH in the pass and within the lagoon. Comparison between SWOT and the Nano-Cyclopée SSH is first carried out over a transect in the Avatoru pass during track 388, cycle 032 (May 11). For this purpose, we extract SWOT SSH values along a predefined transect inside the pass to avoid land-contaminated pixels (Figure 7, black line in left panel). As the tidal range at Rangiroa is small (about 0.25 m), we assume that the temporal variation of the SSH will remain small during the 1-hour boat transect duration. This allows us to compare the temporal SSH values of the Nano-Cyclopée (30 minutes before and after the SWOT overpass) with the quasi-instantaneous SWOT SSH observations (1 s). Figure 7 presents the track of the Nano-Cyclopée in the Avatoru pass (left panel), the measured SSH (middle panel) and SSH residuals (right panel). As we can see in the middle panel, the satellite and in-situ measurements both indicate a strong SSH slope of the order of 9 cm/km across the Avatoru pass. The back (blue) and forth (yellow) measurements present an offset of 3cm on average, which matches well the tidal change measured by the Avatory tide gauge over the same time period (5cm). However, an offset is observed between the instruments, with SWOT presenting a positive bias of 3.6 cm (Table 2) in comparison to the Nano-Cyclopée. The random error given by the CRMSE is relatively low (1.8 cm) indicating excellent performance of SWOT in this very dynamic coastal environment. It is important to note that the tidal currents (flood tide) and wave-current interactions were relatively strong in the pass during the survey, and the performance of the Nano-Cyclopée is certainly degraded in these conditions. Also, due to the proximity to the land, the KaRIn SWH (gridded at 2 km) was not reliable to derive the SSB. We therefore used the Nano-Cyclopée SSH measurements to deduce the SWH along the track, as $SWH = 4 * \sqrt{\sigma_{SSH}}$. Then we recomputed the SSB correction using the KaRIn wind speed.

In addition to this spatial comparison between SWOT and the Nano-Cyclopée in the Avatoru pass, two local comparisons between SWOT and the GNSS buoy inside the Rangiroa lagoon (LAG location in figure 2) are performed using collocated data on May 11 (cycle 032, track 388) and May 15 (cycle 032, track 485). For these comparisons, we compute the SWOT mean SSH and its standard deviation using the nine closest SWOT observations to the buoy location. For these two events, the difference

https://doi.org/10.5194/egusphere-2026-3219
Preprint. Discussion started: 24 June 2026

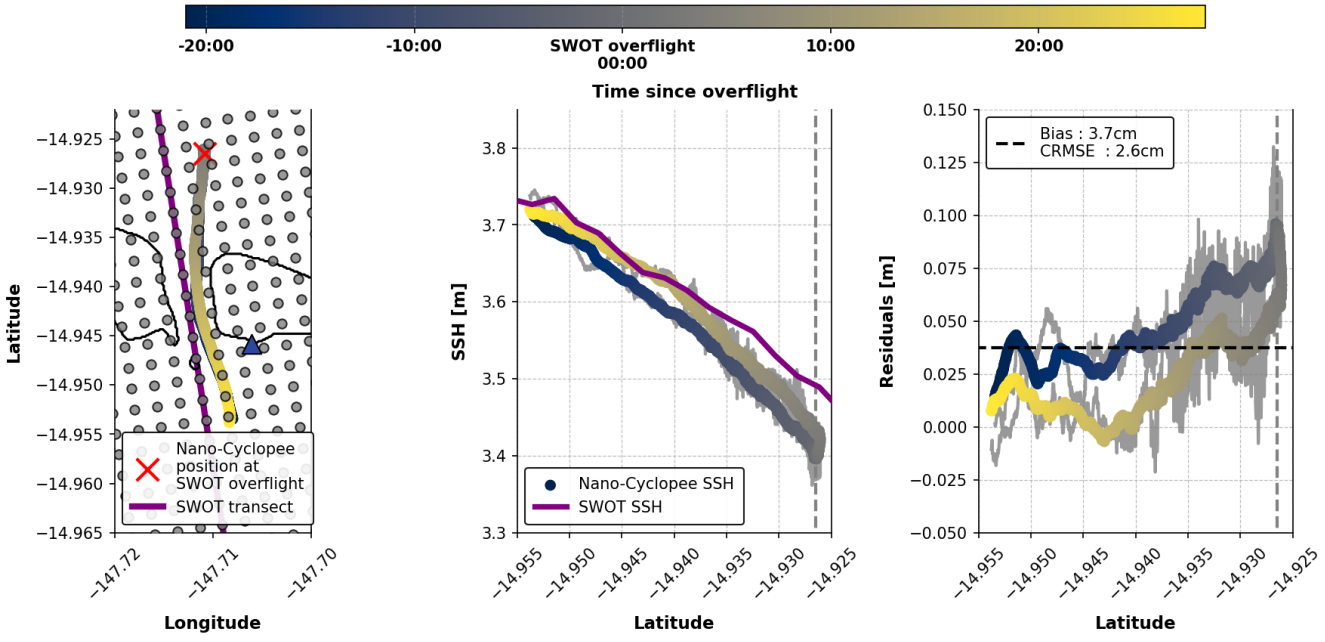

Figure 7. (Left panel) Transect of the Nano-Cyclopée in the Avatoru pass. The color indicates the time relative to the SWOT overflight (May 11, 2025 at 21:11), and the red cross the position of the Nano-Cyclopée during the overflight. The black line represent SWOT points used for this comparison. These points have been chose to minimize the effect of land contamination. The SWOT measurement pixels are displayed in grey dots. (Middle panel) Transect of SSH measured by SWOT (black line) and the Nano-Cyclopée (colored line). The grey line represent the Nano-Cyclopée measurements smoothed on 1-min windows. (Right panel) Residuals between SWOT SSH and the Nano-Cyclopée SSH. The black line represent the bias.

between SWOT SSH and the smoothed (5 minutes) GNSS buoy SSH are -5.2 cm ($\sigma_{SSH,buoy}$ =0.3 cm, $\sigma_{SSH,SWOT}$ =0.8 cm) and 0.7 cm ($\sigma_{SSH,buoy}$ =0.6 cm, $\sigma_{SSH,SWOT}$ = 1.5 cm) respectively (Table 2).

5.3 SWOT SSHA validation

5.3.1 Comparisons of mean SSH profiles

In order to complement the direct validation of SWOT SSH (using SSB_KaRIn) and SWH measurements against in-situ measurements presented in the former subsections, we present here a comparison of SWOT mean SSH against Nano-Cyclopée mean SSH along a transect between Avatoru marina and the LAG station in the lagoon (hereafter referenced as the LAG-AVAT transect and shown on the upper panel of Figure 8) where seven Nano-Cyclopée transects were performed (see Figure 2). The mean SSH is considered here as a proxy for the MSS provided in altimeter products and is therefore also compared to the CNES/CLS MSS provided in SWOT L2 product (version D). Figure 8 shows the MSS from the CNES/CLS model (green curve) and the SWOT mean SSH (orange curve) along the LAG-AVAT transect. Overall, we see a general decreasing

https://doi.org/10.5194/egusphere-2026-3219
Preprint. Discussion started: 24 June 2026

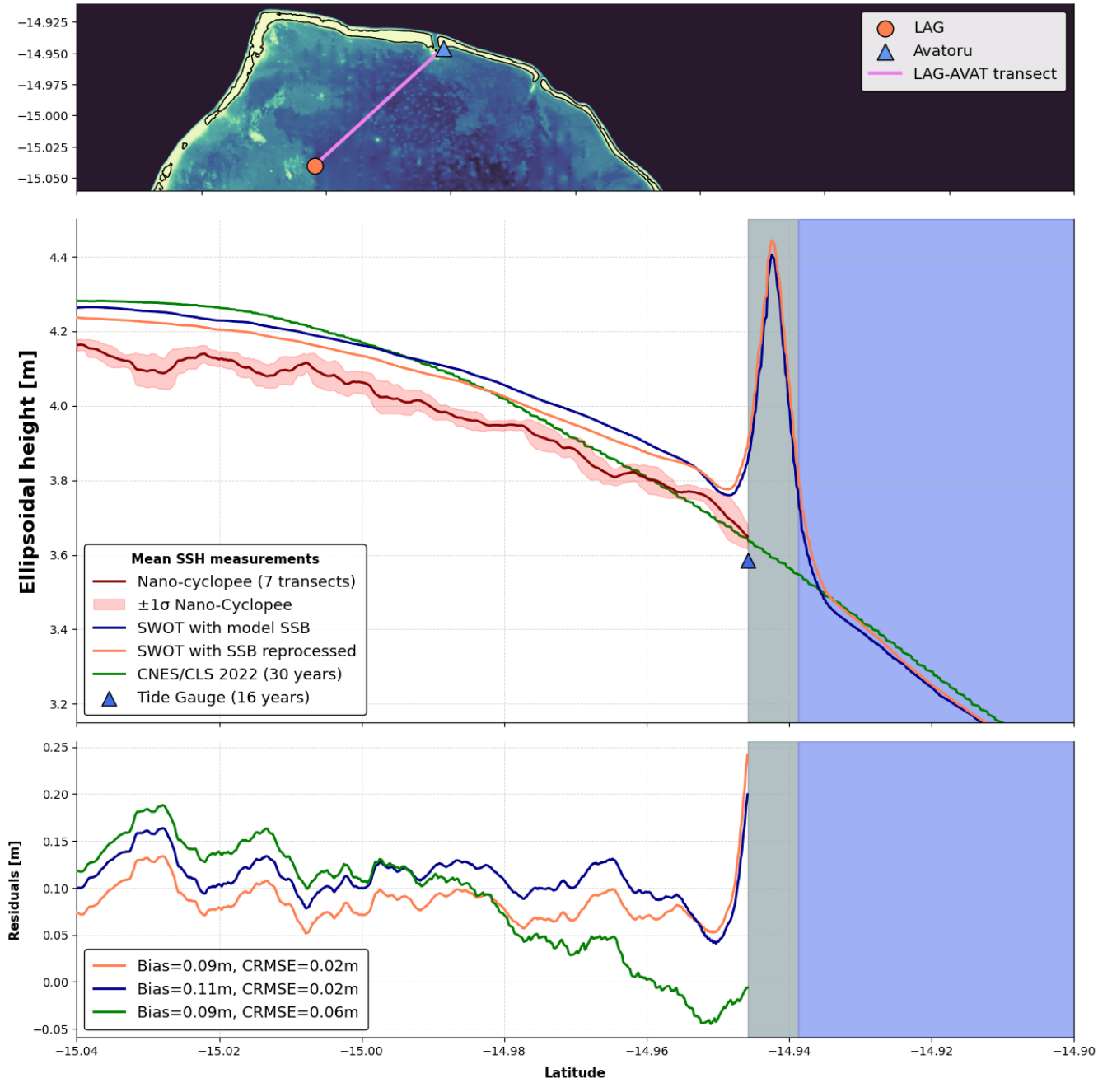

Figure 8. (Upper panel) Localization of the LAG-AVAT transect over the bathymetry maps. (Middle panel) Transect of mean SSH between LAG and Avatoru. Two solutions for SWOT are given. The first (orange) correspond to the mean SSH using the SSB_KaRIn. The second (blue) uses the model-based SSB. The green curve represents the CNES/CLS MSS, and the red one represents the mean SSH estimated by the Nano-Cyclopée. The time coverage of each instrument is indicated in the legend. (Lower panel) Mean SSH residual with respect to the Nano-Cyclopée mean SSH transect.

https://doi.org/10.5194/egusphere-2026-3219
Preprint. Discussion started: 24 June 2026

trend (5cm/km) of the mean SSH from the atoll center to the outer part of the atoll and offshore region, revealing the geoid shape typically induced by seamounts and volcanic islands. But while the two curves are very similar outside the atoll, they clearly show different slopes inside the atoll, with the SWOT mean SSH curve presenting a milder gradient in comparison to the CNES/CLS MSS. Compared to the Nano-Cyclopée mean SSH (red curve), we see that the the trend of the SWOT mean SSH is closer to the in situ observations than the CNES/CLS MSS. This better match between SWOT and in situ observations certainly result from the improved resolution of the KaRIn instrument in comparison to conventional altimeters used to derive the CNES/CLS MSS. However, the SWOT mean SSH also presents a vertical offset of approximately 9 cm in comparison to the in situ measurements, which suggests remaining uncertainties in the geophysical or atmospheric corrections over the atoll. Among these corrections, we expected the SSB correction to be the main contributor. Since the SSB_KaRIn correction is already applied in the SWOT SSH used in this study, we estimate the improvements by comparing it to the SWOT mean SSH using the model-based SSB (blue curve in Figure 8) and we find that the model-based SSB induces an overestimation about 3 cm compared to the SSB_KaRIn. Outside the atoll, where wave models are expected to perform well, the SSB differences reduce to less than 1 cm, highlighting the excellent performance of KaRIn for measuring SWH in open ocean.

Another potential source of errors in these comparisons concerns the different temporal sampling used to compute the SWOT and GNSS-based mean SSH and the CNES/CLS MSS values. Indeed, the acquisition sampling varies from 30 years for the estimate of the CNES/CLS MSS to only a few survey collected within two weeks for the mean SSH Nano-Cyclopée profile. To investigate the impact of the temporal sampling on these mean SSH estimates, the 16-year long tide gauge time-series is used to estimate mean SSH over several time periods: the entire tide gauge time series (from 2009 to 2026), the two-and-a-half-year period of SWOT acquisitions (2023 - 2026), the 80 time of SWOT passes over Rangiroa (ascending and descending tracks and 40 cycles), and finally the seven 30-min chunks in May 2025 during which the AVAT-LAG transect was surveyed with the Nano-Cyclopée. The mean SSH values computed over these different temporal sampling from tide gauge data, are given in Table 3, as well as the difference with respect to the 16-year reference time window. The mean SSH computed over the

Tide gauge temporal sampling	Mean SSH [m]	Residuals [m]
Entire time series (16 years)	3.587	*Reference*
SWOT acquisitions (2.5 years)	3.592	0.006
SWOT cycles (001 to 040)	3.581	-0.005
Nano-Cyclopée tracks	3.597	0.008

Table 3. Mean SSH derived from the tide gauge records using different temporal samplings, with residuals relative to the long-term tide gauge mean (Shom, 2023).

entire time-series is 3.586 m and is equal to the value provided in Shom (2023). Looking at the mean SSH computed over the different temporal sampling, we see that the difference never exceeds 1 cm. The largest error is obtained when the mean SSH is computed over the Nano-Cyclopée acquisition time in May 2025, with difference of 0.8 cm. We can therefore confirm that the differences observed between the CNES/CLS MSS, SWOT mean SSH and the Nano-Cyclopée mean SSH are mostly resulting from instrumental and/or methodological differences rather than temporal sampling.

https://doi.org/10.5194/egusphere-2026-3219
Preprint. Discussion started: 24 June 2026

5.3.2 SSHA field over Rangiroa atoll

A preliminary analysis of the SSHA field from SWOT L2 Unsmoothed Product at Rangiroa revealed significant limitations of this geophysical variable. Namely, the SSHA presented non-realistic features along the atoll rim, with strong gradients located all along the atoll rim inside the lagoon and bulges of large SSHA values in the south-western and eastern part of the lagoons (see left panels and green curves on the right panels of Figure 9). This observation has motivated the development of an improved SSHA field by replacing the provided CNES/CLS MSS with an averaged SSH derived from SWOT Unsmoothed data (see Section 4.1). After assessing the quality of this SWOT mean SSH against CNES/CLS MSS and Nano-Cyclopée mean SSH (Section 5.3.1), we use this product to recompute SSHA fields at Rangiroa, using equation 3. Figure 9 shows the SSHA fields for three cycles (cycle 020/track 485, cycle 008/track 485 and cycle 001/track 485), using the CNES/CLS MSS on one hand (left panels) and the SWOT mean SSH as a proxy for the MSS on the other hand (middle panels). A transect of SSHA is extracted along the main axis of the lagoon in order to highlight the differences in the two SSHA (right panel). When using the SWOT mean SSH as a proxy for the MSS, the SSHA patterns over the atoll appear much more realistic than with the standard product, with sharp SSH gradients between the inner and outer edges of the atoll, which reflect the hydrodynamic behavior of the semi-enclosed system. Two noisy bands are visible either side of the nadir blind zone, as a consequence of degraded SWH acquisitions (used to compute the SSB) in this area. The most striking features are the SSHA offset between the lagoon and offshore water levels, which can be positive or negative and reach up to 50 cm. These differences in water levels result from the delayed tidal wave propagation mainly through the two narrow passes located north of the atoll (Avatoru and Tiputa), which lead to strong tidal asymmetry within the lagoon and time lags up to 3 hours between the high tide, as shown by Postec et al. (2026). Moreover, incident swells breaking over the barrier reefs are known to induce an additional wave setup, which contributes to higher lagoon water levels during period of energetic swells (Sous et al., 2020). Significant differences of the SSHA (up to 15cm) were identified between the southern and northern offshore waters as a potential signature of the tidal wave propagation across the Tuamotu archipelago. Finally, gradients of the order of 5 to 10 cm across the lagoon (not shown here) may result from wind stress, tide propagation or resonant mechanism (seiche) across the lagoon (Rebouillat et al., 2026). Overall, these improved SSHA fields provide an indirect validation of the SWOT-based MSS estimated from the time-averaged Unsmoothed SSH data.

6 Conclusions

The performance of SWOT to measure waves and sea level variability over Rangiroa atoll was investigated using SWH and SSH in situ measurements acquired during a field campaign in May 2025. SWH data were measured with two spotter buoys moored in the western and eastern part of the lagoon, while SSH data were measured at several locations of the lagoon and across the main pass with a GNSS buoy, a Nano-Cyclopée system and a permanent tide gauge. Comparisons between SWOT and Spotter measurements of SWH inside the lagoon indicated a positive bias of SWOT SWH comprised between 10-28cm and CRMSE between 10-13cm for the wind sea conditions observed in the lagoon (SWH ranging from 18cm to 90cm). The largest errors were obtained during the lowest sea state conditions (below 40cm). Comparing these results with

https://doi.org/10.5194/egusphere-2026-3219
Preprint. Discussion started: 24 June 2026

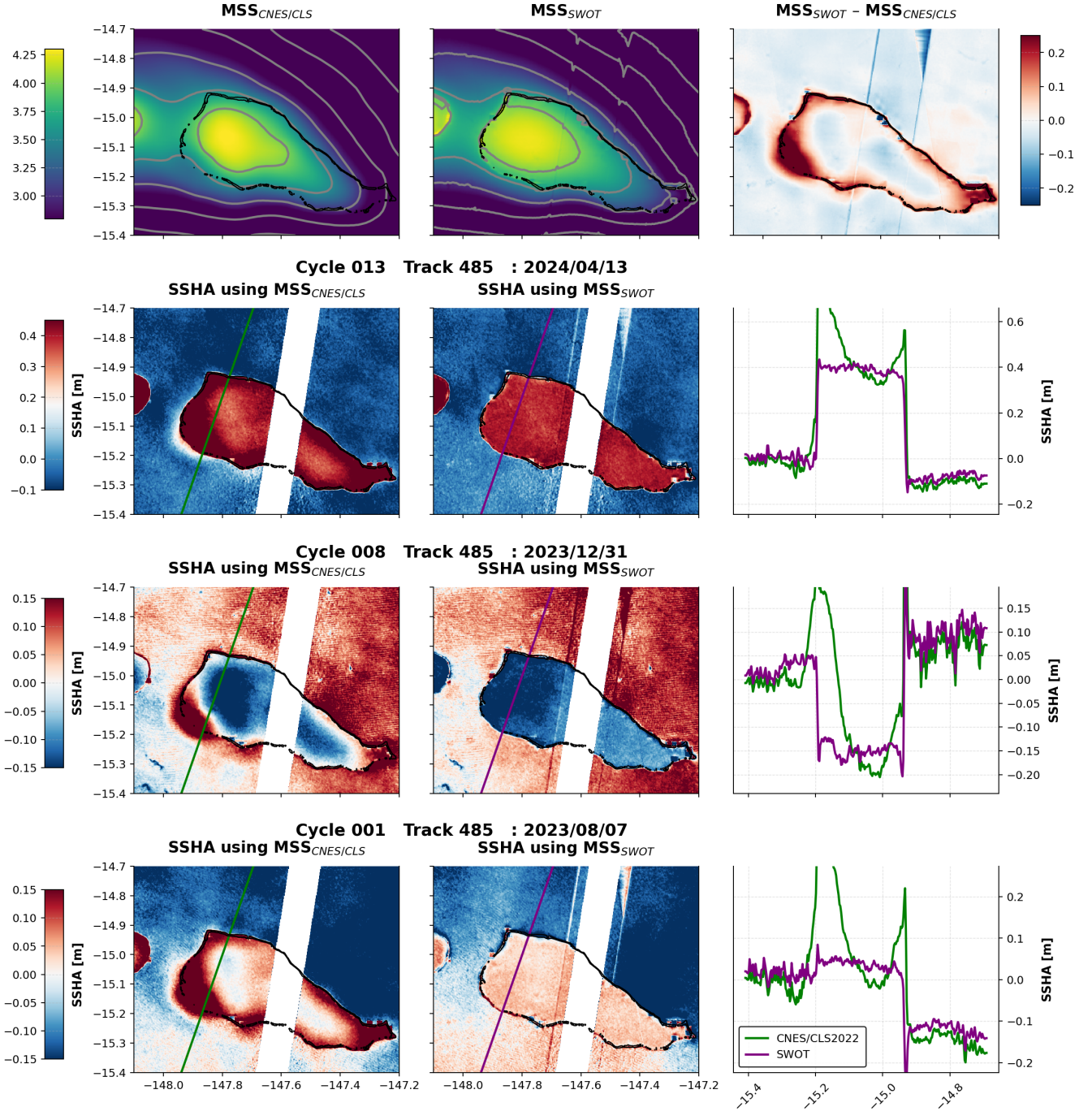

Figure 9. SSHA maps computed using the CNES/CLS 2022 MSS (left column) and using the SWOT mean SSH including the KaRIn sea state bias correction (middle column). The location of the SSHA transects is shown in green (left) and purple (middle). The corresponding SSHA transects are displayed in the right column: the green curve represents the SSHA computed with the CNES/CLS 2022 MSS, and the purple curve represents the SSHA computed with the SWOT mean SSH.

https://doi.org/10.5194/egusphere-2026-3219
Preprint. Discussion started: 24 June 2026

the EC-WAM simulated SWH used in the current L2 SWOT products (version C and D) to correct for sea state bias, SWOT SWH appear to be much more accurate (EC-WAM SWH bias ranges between 105-119cm) and precise (EC-WAM SWH bias ranges between 42-44cm), and was therefore selected to derive an improved SSB, showing SSH error reduction up to 7.5cm. Regarding SSH validation, the comparisons in the lagoon with the GNSS buoy and with the Nano-Cyclopée across the Avatoru pass revealed excellent performance of SWOT KaRIn instrument, with low systematic (bias between -2.25-3.6cm) and random errors (CRMSE between 1.24-1.8cm), while the comparisons with the tide gauge indicated a larger bias (8.6cm) and CRMSE (7.3cm), most pronounced during before and after low tide. While no direct explanation could be found, we expect surface roughness modulation due to wave-current interactions nearby the tide gauge could explain some of the observed errors. Finally, comparisons with repeated Nano-Cyclopée SSH transects within the lagoon showed that the mean sea surface spatial variability was better represented by a mean SSH field directly computed from the SWOT Unsmoothed data than with the CNES/CLS MSS solution, in particular near the atoll edge where the SSH gradients across the pass and SSH offset either side of the atoll barrier can be very sharp. For instance, we monitored with the Nano-Cyclopée instrument a $10cm.km{-}1$ SSH slope across the Avotoru pass, which matched very well the colocated SWOT SSH tracks. Using the new SWOT-based MSS to compute SSH anomaly maps we obtained more realistic pictures of the lagoon dynamics, with very clear differences between the lagoon and offshore water levels, reaching up to 50cm, that result from the time lag of the tidal wave propagation within this semi-enclosed environment, as already evidenced by Postec et al. (2026). In addition, significant differences of the SSHA (up to 15cm) were identified between the southern and northern offshore waters as a potential signature of the tidal wave propagation. Overall, our study provides several recommendations to improve the exploitation of SWOT Level 2 products over atoll islands, and similar coastal systems (e.g. coastal lagoons), through the computation of the SSB and MSS fields based on SWOT Level 2 SWH and SSH measurements. It also highlights the great potential of swath altimetry for investigating the hydrodynamics of large scale atolls with unprecedented level of information regarding the spatial dynamics of these highly complex environments.

Data availability. The SWOT data used in this study are available on the AVISO portal www.aviso.altimetry.fr/. The Avatoru tide gauge data are available on https://data.shom.fr/. The field data collected during the Rangiroa field campaign and analyzed in this study are available upon request to the authors The complete field dataset is being archived on a long term repository (SEANOE) and will be described in a data paper, currently under preparation. The associated DOI will be indicated in this section before final publication.

Appendix

6.1 Uncertainties in GNSS measurements

Uncertainties in SWOT SSH measurements are mostly assessed through comparisons against GNSS measurements (Section 5.2.3 and 5.3.1). For this purpose, we consider the GNSS buoy and Nano-Cyclopée as our reference measurements, neglecting their own uncertainties. However, these measurements are not free of errors and we provide here further information on their

https://doi.org/10.5194/egusphere-2026-3219
Preprint. Discussion started: 24 June 2026

uncertainty levels. The Nano-Cyclopée is composed of two sensors, a GNSS antenna and an acoustic altimeter (see Section 3.1.1). To assess the uncertainty levels of these two instruments, we compute the standard deviation of the raw altitude given by the GNSS antenna/receiver and the air draft measured by the altimeter over 5-min moving windows (referred as $\sigma_{5\mathrm{min}}$). This parameter provides an estimate of the instrumental noise as a function of time (and therefore local conditions). We also compute the mean of $\sigma_{5\mathrm{min}}$ over the full duration of the session (referred as $\overline{\sigma_{5\mathrm{min}}}$) to assess the uncertainty of each sensors over the full session.

We first estimate the uncertainty levels during the cross-validation session held at Avatoru (left panels in Figure 10). During this session, the Nano-Cyclopée (and therefore the GNSS antenna) was set on the ground, so that the uncertainty on the GNSS altitude (i.e. altitude of the antenna reference point) only depends on the instruments and GNSS solution (PPP in the case of this study, see Section 4.3), not on the sea conditions and boat movements. During this session, the $\overline{\sigma_{5min}}$ of the GNSS antenna altitude was very low (1.57 cm), although the 5-min smoothed signal exhibited significant low-frequency variability, with oscillations up to 15 cm. This indicates that the observed variability occurs over periods greater than 5 minutes, highlighting low-frequency positioning errors.

These errors might come from changes in the satellite constellation, errors in atmospheric corrections or limitations of the PPP method. This uncertainty level is also representative of the GNSS buoy, as it is equipped with the same GNSS antenna and receiver, and processed using the same methodology. The raw altimeter measurements exhibit a higher variability ($\overline{\sigma_{5min}}$ = 8.95 cm), which includes the wave and tide surface motions and therefore does not reflect the instrumental noise alone (middle left panel in Figure 10). The SSH measurements that combines both GNSS and altimeter measurements presents a $\overline{\sigma_{5min}}$ = 9.12cm, which mostly results from the wave-contaminated altimeter measurements. Yet we see that the uncertainty on the GNSS altitude is non-negligible and contribute to the overall error in Section 3.2. To illustrate that, we have computed the Nano-Cyclopée SSH using the median value of the GNSS altitude, instead of the time-varying measurements, and the comparison with the tide gauge shows a bias of 0.1 cm and a CRMSE of 1.1 cm (while the time-varying position gave a bias of 0.3cm and a CRMSE of 4 cm), highlighting the excellent performance (precision and accuracy) of the acoustic altimeter.

When set on a boat, the uncertainty level of the Nano-Cyclopée is expected to increase because of wave-induced motions of the boat, the bow wave and vibrations of the boat engine. To investigate these effects, we compute $\sigma_{5\mathrm{min}}$ on GNSS, altimeter and SSH measurements acquired on May 11 2025, while the Nano-Cyclopée was used to measure SSH variability across the Avatoru pass and along the LAG-Avatoru transect (right panels in Figure 10). During this session the $\sigma_{5\mathrm{min}}$ of the GNSS altitude increases to 12.8 cm in average within the lagoon, with a maximum of approximately 40 cm outside the Avatoru pass, when swell waves directly impacted the boat movements (upper right panel in Figure 10, around May 11 at 21:11). With no surprise, the GNSS antenna is highly sensitive to swell. In contrast, the $\sigma_{5\mathrm{min}}$ of the altimeter measurements remains more stable since the boat follows the swell oscillations, with values ranging between 5 to 10 cm (middle right panel in Figure 10). This indicates that the altimeter is less affected by swell but may still be influenced by smaller waves or boat motions. Moreover, these uncertainties are significantly influenced by the boat's velocity, particularly through dynamic effects, for instance when the boat accelerates and gets on plane (visible around 11 May 23:00 and 23:25 in upper and middle panel of Figure 10). These

https://doi.org/10.5194/egusphere-2026-3219
Preprint. Discussion started: 24 June 2026

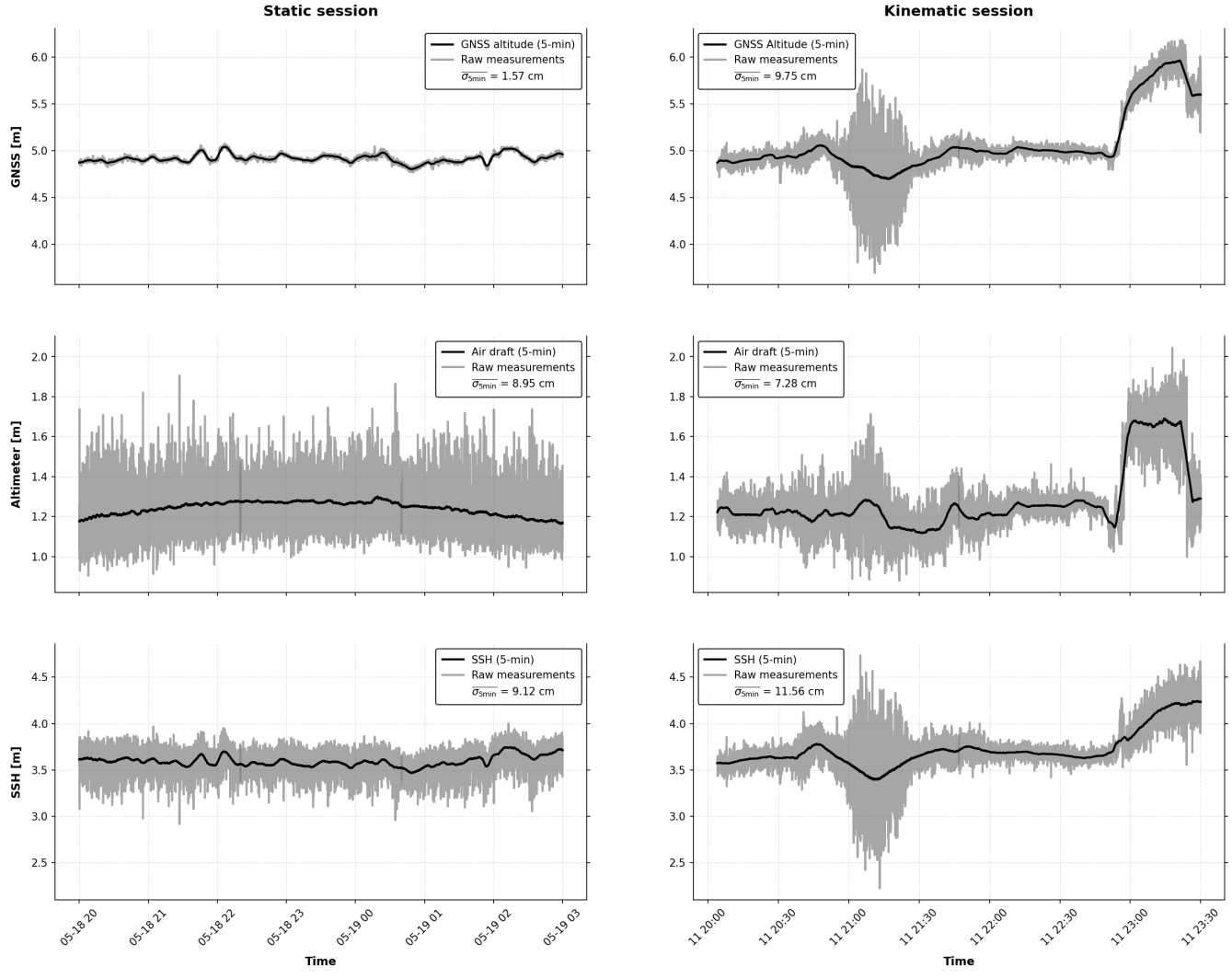

Figure 10. Nano-Cyclopée measurements during the static cross-validation session near the Avatoru tide gauge (left) and during a kinematic session across the Avatoru pass and alongthe LAGA-Avatoru transect (right). (Top panel) GNSS altitude of the Nano-Cyclopée. (Middle panel) Air draft measured by the altimeter. (Bottom panel) Resulting SSH measured by the Nano-Cyclopée. A 5-minutes rolling mean was applied (black line), with the grey shaded areas indicating the raw (1-Hz) records.

https://doi.org/10.5194/egusphere-2026-3219
Preprint. Discussion started: 24 June 2026

rapid GNSS and altimeter changes correspond to changes in the boat's trim and heave, induced by variation in speed and wave interactions, including bow waves.

6.2 PPP vs PPK

In this study, we processed GNSS measurements using the Precise Point Positioning (PPP) method (see section 4.3) using the NRCAN-CSRS tool (Natural Resources Canada, 2024). The PPP method is an absolute positioning method, using atmospheric corrections derived from global models. To reduce bias and variability in our GNSS solutions, we computed GNSS solutions with another positioning method, called Post-Processing Kinematic (PPK), using the RTKLIB software (Takasu, 2013). In contrast to PPP, the PPK method relies on a second GNSS antenna located at a fixed reference position on land. This differential approach allows a better estimation of atmospheric delays compared to model-based corrections. However, the quality of the PPK solution depends on the distance, called baseline, between the rover (here the Nano-Cyclopée or the GNSS buoy) and the permanent GNSS antenna. When this baseline becomes too large, the estimation of atmospheric delays degrades and positioning accuracy decrease. In this study, we used the permanent GNSS antenna installed on the roof of the Avatoru tide gauge (see Section 3.2), with a sampling frequency set at 1 Hz during the campaign. Here we provide further information on the PPK processing results and we compare it to the PPP solutions.

We first defined the RTKLIB PPK processing configuration using the GNSS buoy measurements collected during the calibration session held at Avatoru. During this session, both GNSS instruments were installed near the tide gauge, providing an ideal configuration for the PPK method. We used ultra-precise GRG (*Groupe de Recherche de Géodésie Spatiale*) orbit products from the CDDIS website (https://cddis.nasa.gov/archive/gnss/products/). These orbit products provide orbits with an accuracy of 3 cm (https://igs.org/products/) for GLONASS, GPS and GALILEO constellations. The result is referenced to the ellipsoid ITRF20. Figure 11 shows the SSH time series measured by the tide gauge (black line), by the GNSS buoy with the PPP solution (blue line) and with the PPK solution (orange line). The PPK solution shows an improved precision compared to PPP, with a CRMSE of 0.6 cm for PPK against 2.3 cm for PPP. The accuracy is also improved, with a bias of 2.7 cm for PPK against 4.7 cm for PPP. As presented in Section 4.3, the precision on the measure of the instrumental offset of the buoy is estimated to be 2 cm, which might explain a large fraction of the remaining bias in the PPK solution. We then applied the same configuration to the Nano-Cyclopée measurements, since it is equipped with the same GNSS antenna and receiver. Results are presented in the right panel of Figure 11. The PPK solution also provides a lower overall error for this session, with a CRMSE of 1.8 cm compared to 3.7 cm for the PPP solution. Although the PPP solution exhibits a slightly smaller bias (0.6 cm versus 0.9 cm for the PPK), this likely results from the larger variability of the PPP solution. As expected, the PPK solution performs better than the PPP solution for these two sessions, where the baseline is very short. Also, PPP solutions showed moderate performance for both GNSS instruments during the calibration session. However, using PPK position method shows that both GNSS instruments have a very high level of accuracy and precision compared to the tide gauge. The degraded performances of the PPP solutions can then be attributed to the deployment setup (e.g. masking of the antenna signal reception by the tide gauge building), or the PPP method itself under these conditions.

https://doi.org/10.5194/egusphere-2026-3219
Preprint. Discussion started: 24 June 2026

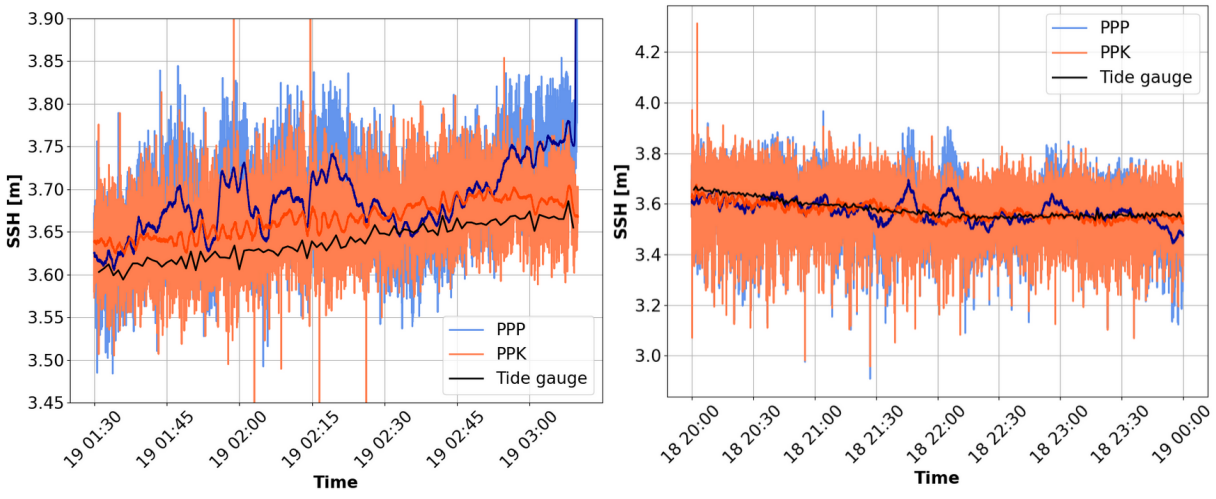

Figure 11. Time series of the SSH measured at Avatoru by the tide gauge (black line), and the GNSS buoy (left panel) or the Nano-Cyclopée (right panel) with the PPP solution (blue line) and the PPK solution (orange line). Pale colors represent the raw measurements, while dark colors represent the 1-min average SSH.

We then applied the same RTKLIB configuration to the GNSS buoy measurements, while it was deployed at LAG (see location in Figure 2). The distance between LAG and the Avatoru permanent GNSS station is around 15 km. Figure 12 shows the SSH time series measured by the GNSS buoy at LAG, with the PPP solution (blue line) and the PPK solution (orange line). During this session, the PPK solution exhibits an important level of noise, with a CRMSE of 70 cm against 8.9 cm for the PPP solution. Yet, the PPK solution shows punctually a good accuracy and precision over small segments, such as May 15 around 10:00. However, overall noise level remains too important at this baseline. As a result, the PPP method is a better choice at this baseline.

Author contributions. GD, CC and LT designed the study and the field campaign. GD, SJ, FB, and and LM conducted the field campaign. EC processed the data. EC and GD wrote the original draft of the paper. Writing (review and editing) was done by CC, LT, TP, LM, SJ and FB. FB, GD and SJ acquired the financial support for the project leading to this publication. All authors have read and agreed to the published version of the article.

Competing interests. The authors declare there are no conflicts of interest for this manuscript

Acknowledgements. The authors would like to thank the many individuals who provided help before, during and after the Rangiroa field campaign: X. Bertin (LIENSs), E. Doerflinger (U. Montpellier), H. Michaud (Shom), and L. Ormières (LIENSs) who participated to the

https://doi.org/10.5194/egusphere-2026-3219
Preprint. Discussion started: 24 June 2026

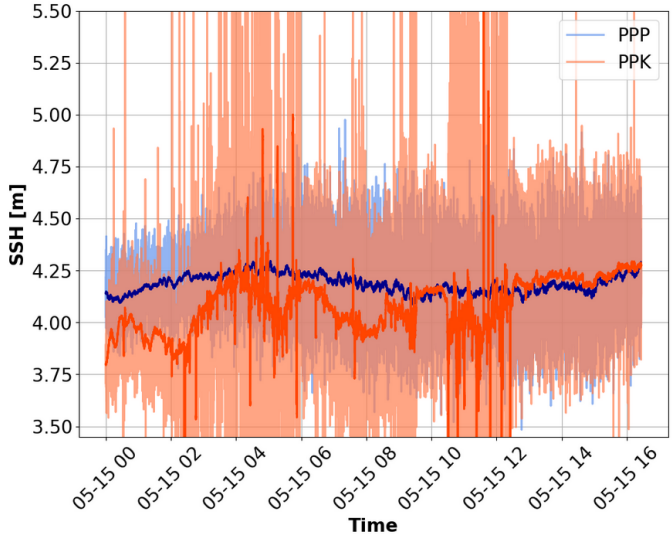

Figure 12. Time series of the SSH measured by the GNSS buoy at LAG, with the PPP solution (blue line) and the PPK solution (orange line). Pale colors represent the raw measurements, while dark colors represent the 1-min average SSH.

deployments during the May 2025 Rangiroa field campaign, the colleagues from LIENSS-DPL team (V. Ballu, T. Coulombier, Audrey Hyeans, D. Dausse and M. Gravelle) who provided the GNSS instruments and helped with the preparation of the GNSS campaign and configurations of the instruments, the colleagues from DT-INSU (L. Fichen and A. Guillot) and LOPS-TOIS team (P. Lebot and S. Leizour) who helped with the technical preparation of the GNSS and Spotter buoy deployments, colleagues from Shom (in particular G. Bertoia) for giving access to the tide gauge facility and maintaining the tide gauge GNSS stations, and finally the many Pa'umotu who contributed to the success of the campaign (in particular Tamatoa, Simeon, Ono, Henriette and Marcel), through their help, kindness and great knowledge of the sea. The Rangiroa field campaign was supported by the French State under the PPR FUTURISKS Project, 'Un Océan de Solutions', managed by the National Research Agency, under France 2030 (ANR-22-POCE-0002, PIs X. Bertin and V. Duvat, from LIENSS) and was coordinated by Frédéric Bouchette (Univ. Montpellier). This work was partly supported (funding of the field deployment and logistics) by the program HYDRAUMATH from the French government, managed by the National Research Agency (ANR) under the France 2030 initiative, grant number ANR-23-EXMA-0007. EC, GD, SJ and LM also acknowledges financial support from the Centre national d'études spatiales (CNES).

https://doi.org/10.5194/egusphere-2026-3219
Preprint. Discussion started: 24 June 2026

References

Altamimi, Z., Rebischung, P., Collilieux, X., Métivier, L., and Chanard, K.: ITRF2020: an augmented reference frame refining the modeling of nonlinear station motions, Journal of Geodesy, 97, 47, https://doi.org/10.1007/s00190-023-01738-w, 2023.

Andréfouët, S., Pagès, J., and Tartinville, B.: Water renewal time for classification of atoll lagoons in the Tuamotu Archipelago (French Polynesia), Coral Reefs, 20, 399–408, https://doi.org/10.1007/s00338-001-0190-9, 2001.

Andréfouët, S., Desclaux, T., Buttin, J., Jullien, S., Aucan, J., Le Gendre, R., and Liao, V.: Periodicity of wave-driven flows and lagoon water renewal for 74 Central Pacific Ocean atolls, Marine Pollution Bulletin, 179, 113 748, https://doi.org/https://doi.org/10.1016/j.marpolbul.2022.113748, 2022.

Andréfouët, S., Bruyère, O., Liao, V., and Le Gendre, R.: Hydrodynamical impact of the July 2022 'Code Red' distant mega-swell on Apataki Atoll, Tuamotu Archipelago, Global and Planetary Change, 228, 104 194, https://doi.org/10.1016/j.gloplacha.2023.104194, 2023.

Bohé, A.: Sea State Bias: current work towards improving the model, SWOT Science Team Meeting, communication orale, 14–17 octobre 2025, 2025.

Bohé, A., Chen, A., Chen, C., Dubois, P., Fore, A., Molero, B., Peral, E., Raynal, M., Stiles, B., Ardhuin, F., Hay, A., Legresy, B., Lenain, L., and Villas Bôas, A. B.: Measuring Significant Wave Height Fields in Two Dimensions at Kilometric Scales With SWOT, IEEE Transactions on Geoscience and Remote Sensing, 63, 1–19, https://doi.org/10.1109/TGRS.2025.3551605, 2025.

Bonnefond, P., Exertier, P., Laurain, O., Thibaut, P., and Mercier, F.: GPS-based sea level measurements to help the characterization of land contamination in coastal areas, Advances in Space Research, 51, 1383–1399, https://doi.org/https://doi.org/10.1016/j.asr.2012.07.007, satellite Altimetry Calibration and Deformation Monitoring using GNSS, 2013.

Bonnefond, P., Exertier, P., Laurain, O., Guinle, T., and Féménias, P.: Corsica: A 20-Yr multi-mission absolute altimeter calibration site, Advances in Space Research, https://doi.org/https://doi.org/10.1016/j.asr.2019.09.049, 25 Years of Progress in Radar Altimetry, 2019.

Bonnefond, P., Laurain, O., Exertier, P., Calzas, M., Drezen, C., Fichen, L., Guillot, A., Guinle, T., and Picot, N.: Towards 0.1mm/yr stability over decades for measuring sea level using tide gauges together with GNSS-based instruments?, Marine Geodesy, 0, 1–30, https://doi.org/10.1080/01490419.2025.2546920, 2025.

Born, G. H., Parke, M. E., Axelrad, P., Gold, K. L., Johnson, J., Key, K. W., Kubitschek, D. G., and Christensen, E. J.: Calibration of the TOPEX altimeter using a GPS buoy, Journal of Geophysical Research: Oceans, 99, 24 517–24 526, https://doi.org/https://doi.org/10.1029/94JC00920, 1994.

Chupin, C., Ballu, V., Testut, L., Tranchant, Y.-T., Calzas, M., Poirier, E., Coulombier, T., Laurain, O., and Bonnefond, P.: Mapping Sea Surface Height Using New Concepts of Kinematic GNSS Instruments, Remote sensing, 12, https://doi.org/10.3390/rs12162656, 2020.

Chupin, C., Ballu, V., Testut, L., Tranchant, Y.-T., and Aucan, J.: Nouméa: a new multi-mission calibration and validation site for past and future altimetry missions?, Ocean Science, https://doi.org/10.5194/os-19-1277-2023, 2023.

Droxler, A. and Jorry, S.: The Origin of Modern Atolls: Challenging Darwin's Deeply Ingrained Theory, Annual review of marine science, 13, https://doi.org/10.1146/annurev-marine-122414-034137, 2020.

Dumas, F., Gendre, R., Thomas, Y., and Andréfouët, S.: Tidal flushing and wind driven circulation of Ahe atoll lagoon (Tuamotu Archipelago, French Polynesia) from in situ observations and numerical modelling, Marine pollution bulletin, 65, 425–40, https://doi.org/10.1016/j.marpolbul.2012.05.041, 2012.

https://doi.org/10.5194/egusphere-2026-3219
Preprint. Discussion started: 24 June 2026

Dutheil, C., AndrefouÃ«t, S., Jullien, S., Le Gendre, R., Aucan, J., and Menkes, C.: Characterization of south central Pacific Ocean wind regimes in present and future climate for pearl farming application, Marine Pollution Bulletin, 160, 111 584, https://doi.org/https://doi.org/10.1016/j.marpolbul.2020.111584, 2020.

Dutheil, C., Jullien, S., Aucan, J., Menkes, C., Le Gendre, R., and Andréfouët, S.: The wave regimes of the Central Pacific Ocean with a focus on pearl farming atolls, Marine Pollution Bulletin, 162, 111 751, https://doi.org/https://doi.org/10.1016/j.marpolbul.2020.111751, 2021.

European Centre for Medium-Range Weather Forecasts (ECMWF): IFS Documentation CY49R1 – Part VII: ECMWF Wave Model, Technical Report / Book Chapter 81629, European Centre for Medium-Range Weather Forecasts, https://doi.org/10.21957/8315ddc858, accessed: YYYY-MM-DD, 2024.

Fu, L.-L. and Cazenave, A.: Satellite Altimetry and Earth Sciences A Handbook of Techniques and Applications, in: International Geophysics, vol. 69, pp. xi–xii, Elsevier, ISBN 978-0-12-269545-2, https://doi.org/10.1016/S0074-6142(01)80145-5, 2001.

Fu, L.-L., Pavelsky, T., Cretaux, J.-F., Morrow, R., Farrar, J. T., Vaze, P., Sengenes, P., Vinogradova-Shiffer, N., Sylvestre-Baron, A., Picot, N., and Dibarboure, G.: The Surface Water and Ocean Topography Mission: A Breakthrough in Radar Remote Sensing of the Ocean and Land Surface Water, Geophysical Research Letters, 51, e2023GL107 652, https://doi.org/10.1029/2023GL107652, 2024.

Gaffet, A., Bertin, X., Sous, D., Michaud, H., Roland, A., and Cordier, E.: A new global high-resolution wave model for the tropical ocean using WAVEWATCH III version 7.14, Geoscientific Model Development, 18, 1929–1946, https://doi.org/10.5194/gmd-18-1929-2025, 2025.

Grimaldi, C. M., Lowe, R. J., Benthuysen, J. A., Green, R. H., Reyns, J., Kernkamp, H., and Gilmour, J.: Wave and Tidally Driven Flow Dynamics Within a Coral Reef Atoll off Northwestern Australia, Journal of Geophysical Research: Oceans, 127, e2021JC017 583, https://doi.org/https://doi.org/10.1029/2021JC017583, e2021JC017583 2021JC017583, 2022.

Hay, A., Watson, C., Legresy, B., King, M., Zhou, B., Beardsley, J., and Bohé, A.: In Situ Geometric Validation of SWOT Satellite Observations in Bass Strait, Australia, Earth and Space Science, 12, e2025EA004 326, https://doi.org/https://doi.org/10.1029/2025EA004326, e2025EA004326 2025EA004326, 2025.

Hoegh-Guldberg, O., Jacob, D., Taylor, M., Bindi, M., Brown, S., Camilloni, I., Diedhiou, A., Djalante, R., Ebi, K., Engelbrecht, F., Guiot, J., Hijioka, Y., Mehrotra, S., Payne, A., Seneviratne, S., Thomas, A., Warren, R., Zhou, G., and Tschakert, P.: Impacts of 1.5ºC global warming on natural and human systems, IPCC, 2018.

Lannuzel, S.: Réseau de marégraphes dans le Pacifique, Tech. rep., Shom, https://refmar.shom.fr/sites/default/files/2024-07/get_file7d0f.pdf, 2010.

Lichtman, I. D., Bell, P. S., Gommenginger, C., Banks, C., Calafat, F. M., Brown, J., and Williams, S. D. P.: Evaluating Water Levels From the Surface Water and Ocean Topography (SWOT) Mission in a Hyper-Tidal Coastal and Estuarine Environment, Earth and Space Science, https://doi.org/https://doi.org/10.1029/2024EA004104, 2025.

Lycourghiotis, S. and Kariotou, F.: he "GPS/GNSS on Boat" Technique for the Determination of the Sea Surface Topography and Geoid: A Critical Review, Coasts, 2, 323–340, https://doi.org/10.3390/coasts2040016, 2022.

Natural Resources Canada: CSRS-PPP: Canadian Spatial Reference System Precise Point Positioning, https://webapp.csrs-scrs.nrcan-rncan.gc.ca/geod/tools-outils/ppp.php?locale=fr, 2024.

Peral, E., Esteban-Fernández, D., Rodríguez, E., McWatters, D., De Bleser, J.-W., Ahmed, R., Chen, A. C., Slimko, E., Somawardhana, R., Knarr, K., Johnson, M., Jaruwatanadilok, S., Chan, S., Wu, X., Clark, D., Peters, K., Chen, C. W., Mao, P., Khayatian, B., Chen, J., Hodges, R. E., Boussalis, D., Stiles, B., and Srinivasan, K.: KaRIn, the Ka-Band Radar Interferometer of the SWOT Mission: Design and

https://doi.org/10.5194/egusphere-2026-3219
Preprint. Discussion started: 24 June 2026

in-Flight Performance, IEEE Transactions on Geoscience and Remote Sensing, 62, 1–27, https://doi.org/10.1109/TGRS.2024.3405343, 2024.

Petit, G. and Luzum, B.: IERS Conventions, Tech. rep., IERS, 2010.

Postec, T., Dodet, G., and Ardhuin, F.: Wave, Wind and Sea Level Observations Across an Atoll Barrier Reef-Lagoon System from Wide Swath Radar Altimetry, in: Coastal Dynamics 2025, edited by Coelho, C., Hallin, C., Sancho, F., and Silva, P. A., pp. 448–454, Springer Nature Switzerland, Cham, ISBN 978-3-032-15477-4, https://doi.org/10.1007/978-3-032-15477-4_68, 2026.

Pujol, M.-I., Schaeffer, P., Faugère, Y., Matthias, R., Didarboure, G., and Picot, N.: Gauging the Improvement of Recent Mean Sea Surface Models: A New Approach for Identifying and Quantifying Their Errors, JGR Oceans, https://doi.org/10.1029/2017JC013503, 2018.

Rebouillat, E., Oruba, L., Hopuare, M., Planes, S., and Dormy, E.: SWOT Sheds Light on Seiche Oscillations Within Atoll Islands, Geophysical Research Letters, 53, e2025GL119 801, https://doi.org/10.1029/2025GL119801, _eprint: https://agupubs.onlinelibrary.wiley.com/doi/pdf/10.1029/2025GL119801, 2026.

Rougerie, F. and Gros, R.: Les courants dans la passe d'Avatoru, Tech. rep., ORSTOM, https://horizon.documentation.ird.fr/exl-doc/pleins_textes/divers09-01/00380.pdf, 1980.

Schaeffer, P., Pujol, I., Veillard, P., Yannice, F., Dagneaux, Q., Gerald, D., and Picot, N.: The CNES CLS 2022 Mean Sea Surface: Short Wavelength Improvements from CryoSat-2 and SARAL/AltiKa High-Sampled Altimeter Data, Remote Sensing, 15, 2910, https://doi.org/10.3390/rs15112910, 2023.

Seifi, F., Deng, X., and Andersen, O. B.: Assessment of the Accuracy of Recent Empirical and Assimilated Tidal Models for the Great Barrier Reef, Australia, Using Satellite and Coastal Data, Remote Sensing, 11, https://doi.org/10.3390/rs11101211, 2019.

Shih, H.-C., Hwang, C., Barriot, J.-P., Mouyen, M., Corréia, P., Lequeux, D., and Sichoix, L.: High-resolution gravity and geoid models in Tahiti obtained from new airborne and land gravity observations: Data fusion by spectral combination Geodesy, Earth Planets and Space, 67, https://doi.org/10.1186/s40623-015-0297-9, 2015.

Shom: Références altimétriques maritimes, https://diffusion.shom.fr/donnees/references-verticales/references-altimetriques-maritimes-ram.html, 2022.

Shom: Fiche d'observatoire de marée – AVATORU LAGON, Internal document provided by SHOM via personal communication, fiche n°3154, mise à jour du 16 février 2023, 2023.

SHOM: REFMAR: Réseau de références marégraphiques, https://doi.org/10.17183/REFMAR#78, tide gauge database, 2024.

Sofar: Spotter SD Card Parser, https://github.com/sofarocean/spotter-sd-parser.git, 2019.

Sofar: Wave Parameter Definitions, Tech. rep., Sofar Ocean, 2021.

Sous, D., Dodet, G., Bouchette, F., and Tissier, M.: Momentum Balance Across a Barrier Reef, Journal of Geophysical Research: Oceans, 125, e2019JC015 503, https://doi.org/https://doi.org/10.1029/2019JC015503, 2020.

Stiles, B., Dubois, P., Bohé, A., and Vadon, H.: SWOT Product Description, Tech. rep., Surface Water and Ocean Topography (SWOT) Project, NASA JPL and CNES, 2022.

Storlazzi, C. D., Elias, E. P. L., Berkowitz, P., Reynolds, M. H., and Gibbs, A. E.: Most atolls will be uninhabitable by the mid-21st century because of sea-level rise exacerbating wave-driven flooding, Nature Communications, 9, 5041, https://doi.org/10.1038/s41467-018-07536-9, 2018.

SWOT Science Team: SWOT Level-2 KaRIn SSH and SWH Data Products, https://doi.org/10.24400/527896/A01-2023.015, 2023a.

SWOT Science Team: SWOT Level-2 KaRIn SSH and SWH Data Products, https://doi.org/10.24400/527896/A01-2023.016, 2023b.

https://doi.org/10.5194/egusphere-2026-3219
Preprint. Discussion started: 24 June 2026

SWOT Science Team: SWOT User Handbook, https://www.earthdata.nasa.gov/s3fs-public/2024-06/D-109532_SWOT_UserHandbook_20240502.pdf, version 1.1, 2024.

Takasu, T.: RTKLIB: An Open Source Program Package for GNSS Positioning, http://www.rtklib.com/, http://www.rtklib.com/, c++ software, Tokyo, Japan, 2013.

Tolman, H. L.: Treatment of unresolved islands and ice in wind wave models, Ocean Modelling, 5, 219–231, https://doi.org/https://doi.org/10.1016/S1463-5003(02)00040-9, 2003.

Tran, N., Labroue, S., Philipps, S., Bronner, E., and Picot, N.: Overview and Update of the Sea State Bias Corrections for the Jason-2, Jason-1 and TOPEX Missions, Marine Geodesy, 33, 348–362, https://doi.org/10.1080/01490419.2010.487788, 2010.

Turki, E., Islam, M., Solano, C. L., Salameh, E., Domingues, M., Mendoza, T., Aouf, L., Froideval, L., Barcelo, D. G., Laignel, B., Carbonniere, A., and Frappart, F.: On the use of SWOT altimetry data for monitoring coastal hydrodynamics, International Journal of Applied Earth Observation and Geoinformation, 145, 104 982, https://doi.org/https://doi.org/10.1016/j.jag.2025.104982, 2025.

Vignudelli, S., Kostianoy, A., Cipollini, P., and Benveniste, J.: Coastal altimetry, Springer, https://doi.org/10.1007/978-3-642-12796-0, 2011.